Permanence of large eddies in Richtmyer–Meshkov turbulence for weak shocks and high Atwood numbers

Olivier Soulard and Jérôme Griffond●
CEA, DAM, DIF, F-91297 Arpajon, France

The purpose of this article is to analyze the large-scale properties of a Richtmyer–Meshkov turbulent mixing zone with large density contrasts and small shock Mach numbers. The main outcome of the study is the expression of a large-scale invariant of the flow. Its existence is contingent on initial conditions but not on the value of the Atwood number which measures the density contrast. As opposed to the small Atwood case, this invariant is not related to the velocity spectrum. Instead, it is given by the value of the spectrum of the solenoidal component of the momentum at small wave numbers. This result stems from the conservation of angular momentum in variable-density flows. Despite this fundamental difference, this invariant still allows to relate the self-similar growth rate of the mixing zone to the large-scale post-shock initial conditions of the flow. Besides, when the shock is weak, this relation can be extended to the pre-shock deformation of the interface. In particular, when the initial interfacial perturbation is limited to small wavelengths (annular spectrum), the growth rate exponent of the mixing zone is shown to saturate to a minimum value close to 1/4, independently from the Atwood number. The different assumptions and predictions of this work are verified by performing implicit large eddy simulations of a Richtmyer–Meshkov turbulent mixing zone.

I. INTRODUCTION

Turbulent mixing zones generated by the Richtmyer–Meshkov instability [1,2] undergo a self-similar evolution at late times [3–6]. During this period, the mixing zone width grows as a power of time, with an exponent Θ that is of paramount importance for engineering applications. Most of the studies dedicated to this asymptotic regime have settled upon the idea that the self-similar properties of the flow, and more particularly the value of Θ, are controlled by the largest scales of the turbulent field (see Refs. [3–6] and references therein). The consensus, however, stops short of specifying how the interplay between large scales and self-similarity occurs and what its outcome is. Several mechanisms detailing these aspects have thus been proposed over the years. They can be divided into two broad categories.

In the first one, the flow is decomposed into linear interfacial modes and one follows their evolution until they reach saturation and give rise to nonlocal structures such as bubbles and spikes. For example, the just-saturated mode theory [7–10] explains how the growth of the mixing zone and the value of Θ are regulated by the linear amplification of modes with wavelengths larger than the size of the mixing zone. In other instances, nonlinear processes, such as bubble mergers [11] or backscattering energy transfers [12], are argued to be the dominant processes. In the first case, Θ is found to depend on initial conditions, whereas, in the second case, its value is predicted to be universal.

In addition to this approach, another line of reasoning has been followed to predict the self-similar properties of Richtmyer–Meshkov turbulence. Instead of describing the flow in terms of a collection of elementary structures, the emphasis is put on statistical quantities, and more especially

on two-point correlations and turbulent spectra. Within this framework, connections with well-established results of turbulence theory can be drawn. In particular, in Refs. [13–15], the principle of permanence of large eddies was transposed from the context of decaying homogeneous turbulence [16–23] to the context of Richtmyer–Meshkov turbulence. This principle details the conditions under which the large-scale part of the velocity spectrum remains constant. When it is verified, a large-scale invariant exists. As a result, the self-similar evolution of the flow is prescribed and the value of Θ can be determined. Note that the statistical and structural viewpoints are not exclusive from one another. On the contrary, the two approaches share many common points and bridges can be built to go from one to the other [15].

Even so, a fundamental hypothesis currently restricts the domain of validity of the principle of permanence of large eddies in the Richtmyer–Meshkov context: the density contrast of the mixing zone is required to be small. Indeed, the analysis performed in Refs. [13–15] expressly rests upon the incompressible Boussinesq approximation. For high-density contrasts, the latter is not valid anymore, so that the derivations proposed in Ref. [13–15] cannot be upheld. Thus, for Richtmyer–Meshkov flows with high density contrasts, the question of whether the principle of permanence of large eddies applies or not remains open.

It turns out that a similar issue has recently been examined in the context of decaying homogeneous variable-density turbulence. In this academic setting, it was shown in Ref. [24] that high density contrasts can be dealt with by looking at the properties of the solenoidal component of the momentum. By considering the spectrum of this quantity instead of the standard velocity spectrum, invariant properties of large scales can be put forward. From there, a principle of permanence of large eddies can be expressed, with only slight modifications with respect to the constant density case. It is worth stressing that, at first sight, the solenoidal momentum might appear as a somewhat peculiar variable. But its definition is in fact anchored to the more tangible concept of angular momentum. The latter notion is at the heart of the analysis of large turbulent scales in constant density flows [18,20,21]. Its appearance in a variable density context can be viewed as a mere prolongation of this pre-existing key role.

Given the analogies that already exist between decaying homogeneous turbulence and Richtmyer–Meshkov mixing zones, the question arises as to whether the results obtained in Ref. [24] can be transposed to the Richtmyer–Meshkov context. The purpose of this work is to answer this question. More precisely, our goal is to determine whether the solenoidal momentum spectrum exhibits invariant properties at large scales for a high-density contrast Richtmyer–Meshkov turbulent mixing zone. And if this is the case, whether these large-scale properties allow us to determine the flow evolution in the self-similar regime. To achieve these objectives, we will combine together two of our previous works: one on Richtmyer–Meshkov turbulence in the Boussinesq limit [15], the other on variable-density homogeneous turbulence [24]. When presenting the results of this combination, we have chosen to make the text as self-contained as possible, instead of systematically deferring the reader to those two earlier works. Even though many elements of Refs. [15,24] are repeated with some slight variations, this solution still looked preferable compared to a lacunar presentation of the main concepts.

The remainder of this article unfolds as follows. First, in Sec. II, we briefly present the variable-density approximation and its corresponding governing equations. Then, in Sec. III, we derive conditions under which the infrared range of the solenoidal momentum spectrum remains permanent. Furthermore, in Sec. IV, we explain how the initial conditions of the solenoidal momentum spectrum are tied to the deformation of the interface. This allows us to discuss in Sec. V how the self-similarity of the flow is influenced by large-scale initial conditions. Finally, elements of validation are provided in Sec. VI.

II. GOVERNING EQUATIONS

We consider two fluids, with densities ρ_H and $\rho_L < \rho_H$, initially separated by a sharp interface. The density contrast between the fluids is possibly large so that the Atwood number A_t is generally

(a) $t = 0$
Interface at rest

(b) $t = t_c$
Shock impact

(c) $t_c < t < t_{qi}$
Compressible phase

(d) $t > t_{qi}$
Quasi-incompressible
phase

(e) $t > t_{ss} > t_{qi}$
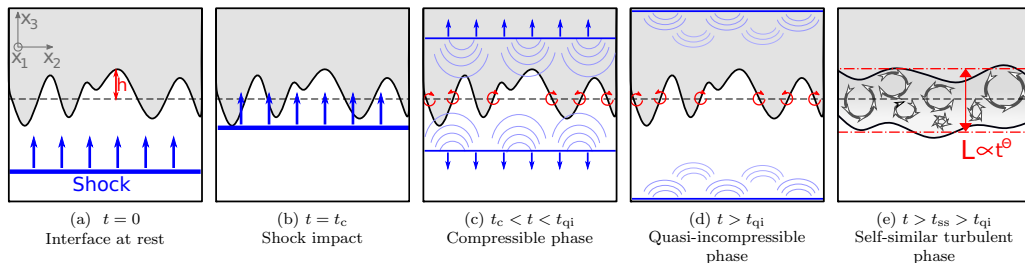Self-similar turbulent
phase

FIG. 1. Schematic representation of the unfolding of the Richtmyer–Meshkov instability. The amplitude of the perturbation in panels (a–d) has been exaggerated to allow for a better visualization of the perturbation. Besides, the width L in panel (e) is much larger than the height h indicated in panel (a). The two figures are not up to scale.

not small:

$$A_t = \frac{\rho_H - \rho_L}{\rho_H + \rho_L} \lesssim 1.$$

A shock is sent towards the interface and crosses it at time t_c. Following the impact, the small perturbations that initially seeded the interface are amplified according to the Richtmyer–Meshkov mechanism [1,2]. This preliminary phase is marked by strong compressible effects. However, as the transmitted shock and its reflected wave travel farther and farther from the interface, these effects fade away until, at time t_{qi}, they can be neglected [25,26]. Eventually, a mixing zone appears and the flow transitions around time $t = t_{ss}$ to a self-similar turbulent state. During the latter phase, the mixing zone width L evolves as a power of time:

$$L = L_0 t^{\Theta}, \tag{1}$$

with L_0 and Θ two constants. These different steps are illustrated in Fig. 1.

In most of this work, we will focus on the flow dynamics once the quasi-incompressible stage $t > t_{qi}$ has been reached. Hence, we will hereafter introduce governing equations that are adapted to this phase. The gap between the flow parameters at $t = 0$ and at $t = t_{qi}$ will be bridged afterwards, in Sec. IV.

A. Variable-density equations

The quasi-incompressible stage $t > t_{qi}$ can be described by the so-called "variable-density" approximation [27–30]. The latter can be thought of as a generalization of the incompressible Boussinesq approximation to flows having a small Mach number but large density contrasts. It belongs to the broader family of pseudocompressible approximations [31]. The variable density approximation can be expressed in terms of the conservation of mass and momentum, with an additional constraint on the velocity divergence:

$$\partial_t \rho + \partial_j (\rho v_j) = 0, \tag{2a}$$

$$\partial_t (\rho v_i) + \partial_j (\rho v_i v_j) = -\partial_i p - \partial_j \sigma_{ij}, \tag{2b}$$

$$\partial_j v_j = \partial_j a_j, \tag{2c}$$

where ∂_j refers to the partial derivative with respect to the coordinate x_j and where ρ is the density, $\boldsymbol{v}$ the velocity, p the pressure and $\boldsymbol{\sigma}$ the viscosity tensor:

$$\sigma_{ij} = -\rho \nu S_{ij} \quad \text{with} \quad S_{ij} = \partial_j v_i + \partial_i v_j - \frac{2}{3} \partial_k v_k \delta_{ij} \quad \text{and} \quad \nu \text{ the kinematic viscosity.}$$

The diffusion velocity $\boldsymbol{a}$ accounts for the effects of molecular transport on the density field. It is defined by

$$a_j = -\nu_c \partial_j \rho / \rho,$$

where ν_c is the diffusion coefficient of the mass fraction c of one of the two fluids being mixed. In agreement with the "variable-density" approximation, the diffusion coefficients and viscosities are functions of the density ρ.

B. Divergence-free formulation

The previous expression of the "variable-density" approximation can be reformulated by introducing a divergence-free velocity field $\boldsymbol{u}$ defined by

$$\boldsymbol{u} = \boldsymbol{v} - \boldsymbol{a}.$$

System Eqs. (2) can then be rewritten as

$$\partial_t \rho + \partial_j(\rho u_j) = \partial_j(\nu_c \partial_j \rho), \tag{3a}$$

$$\partial_t(\rho u_i) + \partial_j(\rho u_i u_j) = -\partial_i p - \partial_j \Sigma_{ij}, \tag{3b}$$

$$\partial_j u_j = 0, \tag{3c}$$

where Σ_{ij} includes various viscous and diffusive effects:

$$\Sigma_{ij} = \sigma_{ij} + \rho a_i u_j + \rho u_i a_j + \rho a_i a_j - \rho(u_k a_k + a_k a_k - \nu_c \partial_k a_k)\delta_{ij}.$$

To satisfy the divergence-free condition on the velocity field, the pressure must obey the following Poisson-like equation:

$$\partial_{jj}^2 p - \partial_i p \frac{\partial_i \rho}{\rho} = -\rho \partial_{ij}^2(u_i u_j) - \partial_{ij}^2 \Sigma_{ij} + \partial_j \Sigma_{ij} \frac{\partial_i \rho}{\rho}. \tag{4}$$

In the constant density case $\rho = \text{Cst}$, this equation becomes $\partial_{jj}^2 p = -\partial_{ij}^2(\rho u_i u_j + \Sigma_{ij})$. By comparing this simplified expression with the full Poisson Eq. (4), one can observe that density variations have a nonnegligible impact on the pressure field. Furthermore, since pressure is a nonlocal quantity, modifications induced by local density variations can affect the pressure field over the whole domain. As discussed in Ref. [24], this nonlocal effect explains how density variations eventually alter the behavior of large turbulent scales.

C. Angular momentum and solenoidal component of the linear momentum

Two interrelated quantities play a role in the forthcoming analysis of large scales: the angular momentum of the flow and the solenoidal component of the linear momentum. In a variable-density flow, angular momentum is tied to the curl of the linear momentum $\rho \boldsymbol{u}$, a quantity that will be denoted as $\boldsymbol{\varpi}$:

$$\varpi_i = \epsilon_{ijk} \partial_j(\rho u_k). \tag{5}$$

with ϵ_{ijk} the Levi-Civita tensor. When density is constant, $\boldsymbol{\varpi}$ is simply proportional to the vorticity field $\boldsymbol{\omega} = \nabla \wedge \boldsymbol{u}$ However, when density varies, the two quantities are in general different $\boldsymbol{\varpi} \neq \rho\boldsymbol{\omega}$. Furthermore, in the same way the vorticity field $\boldsymbol{\omega}$ is connected with the solenoidal component of the velocity field, the angular momentum $\boldsymbol{\varpi}$ is related to the solenoidal part of the momentum through a Biot-Savart expression. More precisely, the Helmholtz decomposition of the momentum takes the form

$$\rho \boldsymbol{u} = \boldsymbol{s} + \boldsymbol{d} \quad \text{with} \quad s_i = \epsilon_{ijk} \partial_j \psi_k \quad \text{and} \quad d_i = -\partial_i \phi, \tag{6}$$

where the scalar and vector potentials ϕ and $\boldsymbol{\psi}$ obey the following constraints:

$$\partial_{jj}^2 \psi_i = -\varpi_i \quad \text{and} \quad \partial_{jj}^2 \phi = -\partial_j(\rho u_j). \tag{7}$$

The quantities $\boldsymbol{s}$ and $\boldsymbol{d}$ are, respectively, the solenoidal and dilatational components of the momentum. As can be seen from Eq. (7), and notwithstanding boundary conditions, $\boldsymbol{s}$ is fully determined by the value of the angular momentum $\boldsymbol{\varpi}$.

The evolution equation of $\boldsymbol{s}$ can be deduced from system Eqs. (3). It takes the form

$$\partial_t s_i + \partial_j(\rho u_i u_j) = -\partial_i \Pi - \partial_j \Sigma_{ij}, \tag{8}$$

where the pseudo-pressure Π enforces the divergence-free condition on $\boldsymbol{s}$:

$$\partial_{jj}^2 \Pi = -\partial_{ij}^2(\rho u_i u_j + \Sigma_{ij}). \tag{9}$$

Comparing Eqs. (3b) and (8), we observe that the evolutions of the total momentum $\rho \boldsymbol{u}$ and of its solenoidal component $\boldsymbol{s}$ are similar except for the presence of distinct pressure terms: p in the first case and Π in the second one. In Eq. (3b), p ensures that $\boldsymbol{u}$ is solenoidal, while in Eq. (8), Π ensures that $\boldsymbol{s}$ is solenoidal. The corresponding Poisson equations for p and Π exhibit two main differences. First, the operator acting on Π in Eq. (9) is a Laplacian, while the one acting on p in Eq. (4) involves another term depending on the product between the pressure and the density gradient. Second, the right-hand side of the equation for Π consists in a term differentiated two times. This "conservative" form is lost in the equation for p. These two elements incur significant differences in the nonlocal behavior of p and Π and by extension in the large-scale properties of $\rho \boldsymbol{u}$ and $\boldsymbol{s}$.

These differences were illustrated in Ref. [24] with a simple example consisting in a single variable-density eddy. This example underlines why the solenoidal momentum $\boldsymbol{s}$—and not the velocity field $\boldsymbol{u}$ nor the total momentum $\rho \boldsymbol{u}$—is associated with the existence of large-scale invariants of the flow.

III. PERMANENCE OF LARGE EDDIES

The principle of permanence of large eddies is one of the cornerstones of the analysis of constant-density homogeneous turbulence [18,20,21]. This principle, which expresses the conditions under which the large-scale initial conditions of the flow are preserved, was adapted to the variable-density context in Ref. [24]. This was achieved by transposing its standard expression, which is based on the velocity spectrum, to a formulation based on the spectrum of the solenoidal momentum $\boldsymbol{s}$.

Our purpose in this section is to ascertain that the same transposition can be applied to Richtmyer–Meshkov turbulence. In particular, we would like to check whether the study of large eddies proposed in Ref. [15] for small-Atwood Richtmyer–Meshkov turbulence can be transposed to the high Atwood number limit when considering the spectrum of $\boldsymbol{s}$.

A. Definition of the spectrum of the solenoidal momentum

Outside the classical framework of homogeneous turbulence, the use of Fourier transforms raises numerous questions. Here, as in Refs. [24,32], we introduce turbulent spectra that are related to the Fourier transform of a two-point correlation tensor. In this way, turbulent spectra keep an interpretation close to the one used in homogeneous turbulence.

To begin with, for any quantity X, we denote by $\overline{X}$ its ensemble mean and by $X' = X - \overline{X}$ its fluctuation. We also assume that the flow is inhomogeneous in the direction x_3 but remains statistically homogeneous and axisymmetric in the directions x_1 and x_2 (see Fig. 1). Then, we introduce the trace of the two-point centered correlations of $\boldsymbol{s}$:

$$R^{\mathrm{so}}(x_3, \boldsymbol{r}, t) = \overline{s_i'(\boldsymbol{x} + {}^{\boldsymbol{r}}\!/_2, t) s_i'(\boldsymbol{x} - {}^{\boldsymbol{r}}\!/_2, t)}.$$

This two-point correlation depends not only on the separation $\boldsymbol{r}$ but also on the inhomogeneous coordinate x_3. Instead of keeping all the information carried by this correlation, we choose to

focus solely on its integral over the inhomogeneous direction. We therefore introduce the following correlation:

$$\mathcal{R}^{\text{so}}(\boldsymbol{r}, t) = \frac{1}{2\pi} \int R^{\text{so}}(x_3, \boldsymbol{r}, t) dx_3.$$

We then define a three-dimensional spectral density by taking the Fourier transform of the previous expression:

$$\mathcal{Q}^{\text{so}}(\boldsymbol{k}, t) = \frac{1}{(2\pi)^3} \int e^{-\imath \boldsymbol{k} \cdot \boldsymbol{r}} \mathcal{R}^{\text{so}}(\boldsymbol{r}, t) d\boldsymbol{r}. \tag{10}$$

This spectral density is directly related to the Fourier transform of the fluctuation of $\boldsymbol{s}$. Indeed, one can show that

$$\mathcal{Q}^{\text{so}}(\boldsymbol{k}, t)\delta(\boldsymbol{k}_\perp - \boldsymbol{k}'_\perp) = \overline{\widehat{s'_i}(\boldsymbol{k}, t)\widehat{s'^*_i}(\boldsymbol{k}', t)} \quad \text{with} \quad \boldsymbol{k}' = (k'_1, k'_2, k_3). \tag{11}$$

In this expression, we used the subscript $\perp$ to refer to the restriction of a given vector to the homogeneous directions x_1 and x_2. For instance, one has

$$\boldsymbol{k}_\perp = (k_1, k_2) \quad \text{and} \quad \boldsymbol{x}_\perp = (x_1, x_2).$$

Finally, the modulus spectrum of $\boldsymbol{s}$ is defined by

$$\mathtt{Q}^{\text{so}}(k, t) = \frac{k^2}{2} \oint \mathcal{Q}^{\text{so}}(\boldsymbol{k}, t) d\tilde{\boldsymbol{k}}, \tag{12}$$

with $\oint \cdot d\tilde{\boldsymbol{k}}$ the integral over the unit sphere, $\tilde{\boldsymbol{k}}$ the direction of the wave vector $\boldsymbol{k}$ and k its modulus:

$$\tilde{\boldsymbol{k}} = \boldsymbol{k}/k \quad \text{and} \quad k = \sqrt{k_i k_i}.$$

The integral of the modulus spectrum is linked to the total variance of the solenoidal momentum as follows:

$$\int_0^\infty \mathtt{Q}^{\text{so}}(k, t) dk = \frac{L}{2\pi} \frac{\langle \overline{s'_i s'_i} \rangle}{2} \quad \text{with} \quad \langle \cdot \rangle = \frac{1}{L} \int \cdot \, dx_3, \tag{13}$$

where L is the size of the mixing zone. The operator $\langle \cdot \rangle$ defines a spatial average over the inhomogeneous direction of the mixing zone.

B. Evolution of the solenoidal momentum spectrum

The solenoidal momentum spectrum being defined, we can now determine its evolution. This can be done by taking the Fourier transform of Eq. (8) and using expression Eq. (11) relating $\mathcal{Q}^{\text{so}}$ to $\widehat{s'}$. These operations are detailed in Appendix A and yield the following result: For $k_\perp \neq 0$,

$$\partial_t \mathtt{Q}^{\text{so}}(k, t) = \mathtt{T}(k, t), \tag{14}$$

$$\text{with} \quad \mathtt{T}(k, t) = k^2 \oint \text{Im}[T(\boldsymbol{k}, t)] dS_k$$

$$\text{and} \quad T(\boldsymbol{k}, t)\delta(\boldsymbol{k}_\perp - \boldsymbol{k}'_\perp) = k_k \overline{\left[\widehat{(\rho u_j)' u'_k} + \widehat{\overline{\rho u_3 u'_k}}\delta_{j3} + \widehat{\Sigma_{jk}}\right](\boldsymbol{k}, t) \, \widehat{s'_j}^*(\boldsymbol{k}', t)}.$$

The structure of this equation is very close to the one obtained in homogeneous turbulence [24]. Moreover, at small wave numbers, the transfer term $\mathtt{T}$, can be simplified under the same set of assumptions as the one used in homogeneous turbulence. A detailed account of these simplifications is given in Appendix A. Here, we will simply point out that the dominant part of $\mathtt{T}$ at small wave numbers comes from quadruple correlations of the form $\overline{\widehat{(\rho u_a)' u'_b}(\boldsymbol{k}, t)\widehat{(\rho u_c)' u'_d}(\boldsymbol{k}', t')}$. The latter can be closed using a distant interaction hypothesis. As illustrated in Fig. 2, if we consider that the spectral densities of $\boldsymbol{u}'$ and $(\rho\boldsymbol{u})'$ have a peak located around a wave number k_{peak}, then the
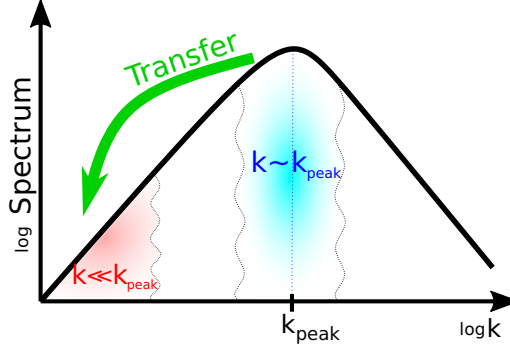
FIG. 2. Schematic representation of the distant interaction hypothesis.

variance of s can be assumed to be transferred preferentially from the region $k \sim k_{\mathrm{peak}}$ to the small wave number region $k \ll k_{\mathrm{peak}}$. This hypothesis eventually leads to the following evolution of $\mathbb{Q}^{\mathrm{so}}$ at small wave numbers (see Appendix A):

$$\text{for } k \ll k_{\mathrm{peak}}(t), \quad \partial_t \mathbb{Q}^{\mathrm{so}}(k,t) = k^4 \, \mathbb{T}^{\mathrm{dist}}(t) + \text{H.O.T.} \tag{15}$$

In this equation, $\mathbb{T}^{\mathrm{dist}}(t)$ arises from the contribution of distant interaction and depends only on time. As for the acronym H.O.T., it stands for higher order terms, it is to say for terms stemming for the next orders of the distant interaction approximation and also from local interactions. In the limit $k \to 0$, these contributions are negligible compared to $k^4 \, \mathbb{T}^{\mathrm{dist}}(t)$ when the infrared exponents of the turbulent spectra are greater than 2. Besides, they are negligible with respect to $\mathbb{Q}^{\mathrm{so}}/\tau_t$, with τ_t the turbulent time, when the infrared exponents are smaller than 2. As a result, they do not play any role in the forthcoming analysis and need not be detailed here.

C. Permanence of large eddies

Knowing the evolution of $\mathbb{Q}^{\mathrm{so}}$, we can now discuss the permanence of large eddies. At time t_{qi}, when the variable density approximation becomes valid, we assume that the spectrum $\mathbb{Q}^{\mathrm{so}}$ satisfies

$$\mathbb{Q}^{\mathrm{so}}(k, t_{\mathrm{qi}}) = C_{\mathrm{so}} k^{\sigma_{\mathrm{so}}}, \tag{16}$$

with C_{so} a constant. We also assume that

$$\sigma_{\mathrm{so}} > -1.$$

Else, $\mathbb{Q}^{\mathrm{so}}(k, t_{\mathrm{qi}})$ ceases to be integrable at $k = 0$ and the variance of s becomes infinite (see Appendix C for a short and speculative discussion about diverging spectra in finite domains). Then, integrating Eq. (15) yields,

$$\text{for } k \ll k_{\mathrm{peak}}(t), \quad \mathbb{Q}^{\mathrm{so}}(k,t) = C_{\mathrm{so}} k^{\sigma_{\mathrm{so}}} + k^4 \int_{t_{\mathrm{qi}}}^{t} \mathbb{T}^{\mathrm{dist}}(t') dt' + \text{H.O.T.},$$

where H.O.T. stands for quantities with a scaling steeper than either $k^{\sigma_{\mathrm{so}}}$, k^4, or both. Thus, the comparison of the infrared exponents of the different terms on the right-hand side of this equation allows to conclude that the following properties are verified in the limit $k \to 0$:

(1) if $\sigma_{\mathrm{so}} < 4$, $\mathbb{Q}^{\mathrm{so}}$ becomes equal to its initial condition and is consequently permanent,

(2) if $\sigma_{\mathrm{so}} > 4$, the nonlinear backscattering term is dominant so that $\mathbb{Q}^{\mathrm{so}}$ tends to a spectrum with an infrared exponent of 4,

(3) if $\sigma_{\mathrm{so}} = 4$, the infrared exponent of $\mathbb{Q}^{\mathrm{so}}$ is not changed, but the prefactor of $\mathbb{Q}^{\mathrm{so}}$ varies in time.

In homogeneous turbulence, the transition between the backscattering and permanent behavior of large scales is not sharp but occurs within a small interval centered around $\sigma_{\mathrm{so}} = 4$. In practice, the

permanence of large eddies appears to be verified for infrared exponents below 3.5 and not 4 [23,33–35]. A similar transitional interval can also be expected for Richtmyer–Meshkov turbulence. Then, a strict permanence of large eddies is likely to be observed only for infrared exponents verifying

$$\sigma_{so} \leqslant 4 - \eta,$$

with η a parameter on the order of 0.5. The current theory cannot predict the precise value of η and only simulations may provide more information about it.

This series of statements constitutes one of the main result of this work. They express the principle of permanence of large eddies for Richtmyer–Meshkov flows in the high Atwood variable density limit. This principle takes the same form as the one obtained in Ref. [15] for Richtmyer–Meshkov flows in the small Atwood Boussinesq limit, except that the velocity spectrum has been replaced with the solenoidal momentum spectrum Q^{so}. Besides, it also takes a form similar to the one obtained in Ref. [24] for variable-density homogeneous turbulence except for the slightly different definition of the spectrum Q^{so} due to the inhomogeneity of the flow.

IV. INITIAL CONDITIONS

Up to this point, we showed that the large-scale initial condition of Q^{so}, the spectrum of the solenoidal momentum s, is preserved provided its infrared exponent is smaller than $4 - \eta$. However, the notion of initial condition is here ambiguous. Indeed, the large-scale analysis of Sec. III applies to flows obeying the quasi-incompressible variable-density approximation [27–30]. But as explained in Sec. II, and as summarized in Fig. 1, this approximation is only relevant to Richtmyer–Meshkov turbulent mixing zones after the shock is sufficiently far to guarantee that compressible and acoustic effects have become negligible [25,26]. By contrast, these effects play an essential role in the early stages of the Richtmyer-Meshkov instability. As a result, the variable-density approximation and the analysis of Sec. III are inadequate to describe these preliminary phases. This observation raises the question of how can one relate the quasi-incompressible initial state of Q^{so} to the initial properties of the shock and of the interface it crosses. An answer to this question can be brought in two steps. First, with $t = t_c$ the crossing time of the shock and with $t = t_{qi} > t_c$ the beginning of the quasi-incompressible period, we can look at how $Q^{so}(\boldsymbol{k}, t_{qi})$ is related to $Q^{so}(\boldsymbol{k}, t_c)$. Then, we can elaborate on how $Q^{so}(\boldsymbol{k}, t_c)$ is related to the shock and interface characteristics. Concerning the first point, we note that the time t_{qi} marking the beginning of the quasi-incompressible period depends mostly on the shock intensity. For weaker shocks, the decay of pressure and density perturbations related to the shock propagation is faster relatively to the linear growth time of the instability [26]. Concerning the second point, we note that vorticity is deposited by the shock at the interface and in the bulk of the flow. However, the latter contribution becomes negligible when the shock is weak. Given these elements, and to simplify our analysis, we will limit our attention to shocks weak enough for the growth of the interface perturbations to be in a linear regime at $t = t_{qi}$ and weak enough for the vorticity to be deposited predominantly at the interface.

Thus, if M_S refers to the shock Mach number then the ensuing discussion on initial conditions is restricted to the case

$$M_S - 1 \ll 1. \tag{17}$$

In practice shocks are considered to be weak up to $M_S \approx 1.2$. We would like to stress that this condition does not modify the results which have been obtained in Sec. III and which remain valid for $t > t_{qi}$, independently from the value of the shock Mach number.

A. Evolution of Q^{so} from $t = t_c$ to $t = t_{qi}$

Under the weak shock condition Eq. (17), the flow evolves linearly from the shock impact at $t = t_c$ up to the time t_{qi} when the flow becomes quasi-incompressible. Thus, from $t = t_c$ to $t = t_{qi}$, the linear theory of Wouchuk and coworkers is relevant for describing the flow [25,26]. One of the

main results obtained by these authors is expressed in Eq. (7) of Ref. [26] and is repeated here for the sake of completeness:

$$\text{Eq. (7) of Ref. [26]:} \quad \rho_{af}\left(\delta v_{ya}^\infty - \delta v_{ya}^0\right) = \rho_{bf}\left(\delta v_{yb}^\infty - \delta v_{yb}^0\right),$$

where, using the notations of Ref. [26], ρ_{af} and ρ_{bf} are the densities of the two fluids after the shock crossing, where δv_{ya} and δv_{ya} are the velocities parallel to the interface, where the superscript 0 corresponds to the instant just after the shock impact and the superscript ∞ to an asymptotically long time. This equation can be rewritten by putting the initial and final times on the same sides of the equalities. This yields

$$\Gamma_\rho^\infty = \Gamma_\rho^0, \quad \text{with} \quad \Gamma_\rho = \rho_{bf}\delta v_{yb} - \rho_{af}\delta v_{ya}. \tag{18}$$

Therefore, Wouchuk and coworkers show that during the linear phase of the Richtmyer-Meshkov instability Γ_ρ is an invariant quantity and is set by its initial value right after the shock passage. The quantity Γ_ρ is nothing more than the density-weighted circulation based on the momentum $\rho\boldsymbol{u}$. In other words, Eq. (18) expresses the conservation of $\boldsymbol{\varpi}$ at the interface during the linear phase of the flow evolution. Hence, during the linear stage of the Richtmyer-Meshkov instability, one deduces, in agreement with Ref. [26] and Eq. (18) that

$$\text{Linear phase:} \quad \partial_t \boldsymbol{\varpi} = 0. \tag{19}$$

As detailed in Sec. II, the density-weighted vorticity $\boldsymbol{\varpi}$ directly sets the value of the solenoidal momentum $\boldsymbol{s}$ [see Eqs. (6) and (7)]. As a result, the latter is also a linear invariant of Richtmyer-Meshkov turbulence and so is its spectrum $\mathtt{Q}^{\text{so}}$:

$$\text{Linear phase:} \quad \partial_t \boldsymbol{s} = 0 \quad \text{and} \quad \partial_t \mathtt{Q}^{\text{so}} = 0. \tag{20}$$

Thus, we can write that

$$\mathtt{Q}^{\text{so}}(k, t_{\text{qi}}) = \mathtt{Q}^{\text{so}}(k, t_{\text{c}}). \tag{21}$$

The value of $\mathtt{Q}^{\text{so}}$ at the beginning of the quasi-incompressible stage of the flow evolution is equal to its value just after the shock impact. The idea is now to relate this value to the characteristics of the shock and of the interface. Before that, let us note that the constancy of $\boldsymbol{\varpi}$ and $\boldsymbol{s}$ in the linear phase can also be derived by considering directly the evolution equations of $\boldsymbol{\varpi}$ and $\boldsymbol{s}$. The evolution of $\boldsymbol{s}$ is given by Eq. (8) while the evolution of $\boldsymbol{\varpi}$ takes the following form:

$$\partial_t \varpi_i + u_l \partial_l \varpi_i = \frac{\varpi_j}{\rho}\partial_j(\rho u_i) - \frac{\varpi_i}{\rho}\partial_j(\rho u_j) - \epsilon_{ijk}\frac{\partial_j \rho}{\rho}\partial_l(\rho u_k u_l) - \partial_{jl}^2(\epsilon_{ijk}\Sigma_{kl}). \tag{22}$$

Neglecting viscous effects, Eqs. (8) and (22) only contain nonlinear quadratic terms. In the frame moving at the post-shock velocity, and in the linear phase, these quadratic terms become negligible. This directly leads to Eqs. (19) and (20).

B. Initial value of $\mathtt{Q}^{\text{so}}$ at $t = t_{\text{c}}$

As already explained, the shock passage creates angular momentum not only at the interface between the fluids but also in their bulk. However, under the weak shock condition Eq. (17), the bulk contribution becomes negligible and the flow is fully determined by the angular momentum deposited at the interface. In the linear regime, this interfacial contribution can be estimated by using the impulsive approximation first proposed by Richtmyer [1]. An important aspect of this approximation is that the angular momentum becomes proportional to the cross-product between the shock normal, $\boldsymbol{x}_3$, and the gradient of density, or equivalently, the gradient of the concentration c of one of the fluids. The latter condition can be written as

$$\varpi_i(\boldsymbol{x}, t_{\text{c}}) = -r_\varpi\, \varepsilon_{ij3}\, \partial_j c(\boldsymbol{x}, t_{\text{c}}),$$

or equivalently in spectral space

$$\widehat{\varpi}_i(\boldsymbol{k}, t_c) = -\imath\, r_\varpi\, \varepsilon_{ij3}\, k_j\, \widehat{c}(\boldsymbol{k}, t_c).$$

The prefactor r_ϖ is associated with the linear growth rate of the perturbation. For a weak shock, we can use the following estimate, obtained from the impulsive approximation of the Richtmyer–Meshkov instability:

$$r_\varpi = \Delta\rho^+ \Delta U,$$

with $\Delta\rho^+$ the difference between the post-shock densities and ΔU the interface velocity jump due to the shock. Other more refined estimates could also be used but are not necessary in this work [36]. Knowing the value of $\boldsymbol{\varpi}$ at the interface, we can determine the expression of the solenoidal momentum $\boldsymbol{s}$. Using its definition Eq. (6), we find that

$$\widehat{s}_i(\boldsymbol{k}, t_c) = \imath \varepsilon_{ijk}\frac{k_k}{k^2}\,\widehat{\varpi}_j(\boldsymbol{k}, t_c) = (\Delta\rho^+\Delta U)P_{i3}(\tilde{\boldsymbol{k}})\,\widehat{c}(\boldsymbol{k}, t_c), \tag{23}$$

where P_{ij} is the projector on incompressible fields:

$$P_{ij}(\tilde{\boldsymbol{k}}) = \delta_{ij} - \tilde{k}_i\tilde{k}_j, \tag{24}$$

with $\tilde{\boldsymbol{k}} = \boldsymbol{k}/k$ the wave vector direction. Injecting this expression into the definition Eq. (11) of the spectral correlation $\mathcal{Q}^{\text{so}}$, we deduce that

$$\mathcal{Q}^{\text{so}}(\boldsymbol{k}, t_c) = (\Delta\rho^+\Delta U)^2 E_{cc}(\boldsymbol{k}, t_c)P_{33}(\tilde{\boldsymbol{k}}), \tag{25}$$

where E_{cc} is the spectral density of the concentration field: $E_{cc}(\boldsymbol{k}, t)\delta(\boldsymbol{k}_\perp - \boldsymbol{k}'_\perp) = \overline{\widehat{c'}(\boldsymbol{k}, t)\widehat{c'}^*(\boldsymbol{k}', t)}$, with $\boldsymbol{k}' = (k'_1, k'_2, k_3)$.

To close the expression of $\mathcal{Q}^{\text{so}}(\boldsymbol{k}, t_c)$, we need to determine the value of $E_{cc}(\boldsymbol{k}, t_c)$. As shown in Ref. [15], the latter is directly related to the properties of the interface. More precisely, let us consider an interface that displays before the shock passage a small displacement with respect to the position $x_3 = 0$. This displacement is described by the height function $h(\boldsymbol{x}_\perp)$, with $\boldsymbol{x}_\perp = (x_1, x_2)$ the position in the plane perpendicular to x_3 (see Fig. 1). The statistics of $h(\boldsymbol{x}_\perp)$ are assumed to be homogeneous and isotropic, with a zero mean. They are further characterized by the power spectrum $P_h(k_\perp)$ which depends on the 2D planar wave number $k_\perp$. The integral of $P_h(k_\perp)$ is by definition equal to the variance of the perturbation amplitude:

$$\overline{h^2} = \int_0^\infty P_h(k_\perp)dk_\perp.$$

Let us denote by U_s the shock celerity, relative to the interface, before interaction and by ΔU the interface velocity jump due to the interaction. Just after shock, at $t = t_c$, the interface is compressed by a factor $\mathcal{C} = 1 - \Delta U/U_s$. The interface perturbation at $t = t_c$ is then $h^+(\boldsymbol{x}_\perp) = \mathcal{C}h(\boldsymbol{x}_\perp)$ and its spectrum is

$$P_h^+(k_\perp) = \mathcal{C}^2 P_h(k_\perp).$$

Note that this relation is meaningful in the present context because the shock is weak. In that case, the compression factor $\mathcal{C}$ remains close to 1. If a stronger shock had to be considered, the relation between P_h^+ and P_h would have to be modified to accommodate for a more accurate impulsive theory such as the one proposed in Ref. [36].

For a nondiffuse interface, it was shown in Ref. [15] that $E_{cc}(k, t_c)$ and P_h^+ are related at large scales by,

$$\text{for } k\sqrt{\overline{h^2}} \ll 1, \quad E_{cc}(\boldsymbol{k}, t_c) = \frac{1}{(2\pi)^3}\frac{P_h^+(k_\perp)}{k_\perp}. \tag{26}$$

The derivation of this result is repeated in Appendix B, with additional elements concerning the case when the perturbation is Gaussian. Injecting this result into Eq. (25) and integrating over angles, we obtain the following expression for the solenoidal momentum modulus spectrum:

$$\text{For } k\sqrt{\overline{h^2}} \ll 1, \quad \mathbb{Q}^{\text{so}}(k, t_{\text{c}}) = \frac{k^2 (\mathcal{C}\Delta\rho^+\Delta U)^2}{2(2\pi)^3} \oint \frac{P_h(k_\perp)}{k_\perp} P_{33}(\tilde{\boldsymbol{k}}) dS_k. \quad (27)$$

Of particular interest to us is the case when P_h obeys a power law at large scales,

$$\text{for } k_\perp\sqrt{\overline{h^2}} \ll 1, \quad P_h(k_\perp) = Ck_\perp^m, \quad (28)$$

with C a constant. Then, Eq. (27) becomes,

$$\text{for } k\sqrt{\overline{h^2}} \ll 1, \quad \mathbb{Q}^{\text{so}}(k, t_c) = \gamma_m C (\mathcal{C}\Delta\rho^+\Delta U)^2 k^{m+1}, \quad (29)$$

with $\gamma_m = [\sqrt{\pi}\Gamma((m+3)/2)]/[2(2\pi)^2\Gamma((m+4)/2)]$.

It is worth stressing that these formulas are meaningful as long as $\overline{h^2}$ remains finite. When the domain is infinite, P_h must consequently be integrable when $k_\perp \to 0$. In turn, this condition requires the exponent m to be larger than -1. When the domain is finite, these constraints do not apply and the case $m < -1$ can be dealt with. Indeed, there exists a cutoff wave number k_c below which all spectra become null. As a result, provided $k_c\sqrt{\overline{h^2}}$ is much smaller than 1, Eqs. (28) and (29) remain valid in the interval $k_c\sqrt{\overline{h^2}} \leqslant k\sqrt{\overline{h^2}} \ll 1$. Moreover, according to Eq. (29), if m is larger than -2, then $\mathbb{Q}^{\text{so}}$ has an infrared exponent larger than -1. Therefore, it remains integrable when $k \to 0$ and we may consider the properties of $\mathbb{Q}^{\text{so}}$ in the limit $k_c\sqrt{\overline{h^2}} \to 0$ without introducing any divergence. In particular, the discussion led so far about the permanence of large eddies can be applied without any change. Thus, under this interpretation, the validity of Eq. (29) can be extended in the limit $k_c\sqrt{\overline{h^2}} \to 0$ to exponents verifying

$$m > -2.$$

C. Summary

Combining Eqs. (21) and (29), we deduce that, at the beginning of the quasi-incompressible phase, the solenoidal momentum spectrum $\mathbb{Q}^{\text{so}}$ can be expressed as,

$$\text{for } k\sqrt{\overline{h^2}} \ll 1, \mathbb{Q}^{\text{so}}(k, t_{\text{qi}}) = C_{\text{so}}k^{\sigma_{\text{so}}}, \quad \text{with} \quad \sigma_{\text{so}} = m + 1 \quad \text{and} \quad C_{\text{so}} = \gamma_m C (\mathcal{C}\Delta\rho^+\Delta U)^2. \quad (30)$$

It shows that $\mathbb{Q}^{\text{so}}(k, t_{\text{qi}})$ obeys a power law at large scales, with an infrared exponent σ_{so} and a prefactor C_{so} which are directly set by the characteristics of the shock and by the initial interfacial perturbation. We recall that this expression is valid provided $m > -2$, or equivalently provided that

$$\sigma_{\text{so}} > -1.$$

This condition is identical to the one introduced in Sec. III to analyze the permanence of large eddies. Some conjectures about what may occur when $\sigma_{\text{so}} < -1$ are presented in Appendix C.

It is also worth noting that if we attempted to find the value of the velocity spectrum at $t = t_{\text{qi}}$, we would face a major difficulty. Indeed, as opposed to s, $\boldsymbol{u}$ is not invariant during the linear phase. Therefore, even though the velocity spectrum at $t = t_{\text{c}}$ can be related to the characteristics of the initial interface, its value at $t = t_{\text{qi}}$ is modified by linear processes and, among others, is dependent on the arbitrary time interval $t_{\text{qi}} - t_{\text{c}}$. This, as already explained, is not the case for s and $\mathbb{Q}^{\text{so}}$. Thus, the solenoidal momentum and its spectrum have remarkable properties not only during the quasi-incompressible phase of the Richtmyer–Meshkov instability, but also during its linear compressible phase.

V. SELF-SIMILAR EVOLUTION

In Sec. IV, we established that the solenoidal momentum spectrum $\mathbb{Q}^{\text{so}}$ is constant during the early compressible stage of the Richtmyer–Meshkov instability. In Sec. III, we showed that during the subsequent stage, the large-scale part of $\mathbb{Q}^{\text{so}}$ remains invariant if its infrared exponent σ_{so} is smaller than $4 - \eta$. As a result, the post-shock large-scale initial condition of $\mathbb{Q}^{\text{so}}$ is preserved throughout the flow evolution, provided its infrared exponent σ_{so} is smaller than $4 - \eta$. The aim of this section is to indicate how the persistence of this initial information influences the self-similar evolution of the flow, and in particular, how it sets the value of Θ.

A. Value of Θ

In this section, we assume that $t > t_{\text{ss}}$ and that the flow is self-similar, an assumption that has not been required so far. In particular, we assume that the shape of the spectrum $\mathbb{Q}^{\text{so}}$ is self-similar at large and energetic scales. Small scales are not required to obey this condition as long as they marginally contribute to the integral of $\mathbb{Q}^{\text{so}}$ over k. More precisely, knowing that [see Eq. (13)]:

$$\int_0^\infty \mathbb{Q}^{\text{so}}(k,t)dk = \frac{L}{2\pi} \frac{\langle \overline{s_i' s_i'} \rangle}{2},$$

we assume that, at least for large and energetic scales,

$$\text{for } k \lesssim k_{\text{peak}}(t), \quad \mathbb{Q}^{\text{so}}(k,t) = \frac{L(t)}{2\pi} \frac{\langle \overline{s_i' s_i'} \rangle(t)}{2} F[k/k_{\text{peak}}(t)],$$

where F is a given function defining the self-similar shape of the spectrum. Introducing a small parameter $\epsilon \ll 1$, these assumptions eventually lead us to write that

$$\int_0^{\epsilon k_{\text{peak}}} \mathbb{Q}^{\text{so}}(k,t)dk \propto \frac{L}{2\pi} \frac{\langle \overline{s_i' s_i'} \rangle}{2}.$$

In Sec. III, we saw that when $-1 < \sigma_{\text{so}} < 4 - \eta$, large eddies are permanent. In that case, we have $\mathbb{Q}^{\text{so}}(k,t) = C_{\text{so}} k^{\sigma_{\text{so}}}$ in the range $k \leqslant \epsilon k_{\text{peak}}$. Therefore, we can write that,

$$\text{for } -1 < \sigma_{\text{so}} < 4 - \eta, \quad \frac{L}{2\pi} \frac{\langle \overline{s_i' s_i'} \rangle}{2} \propto \int_0^{\epsilon k_{\text{peak}}} C_{\text{so}} k^{\sigma_{\text{so}}} dk \quad \propto \quad k_{\text{peak}}^{\sigma_{\text{so}}+1}.$$

Besides, in the self-similar regime, dimensional arguments allow us to write that

$$L \propto k_{\text{peak}}^{-1} \propto t^\Theta \quad \text{and} \quad \langle \overline{s_i' s_i'} \rangle \propto t^{2\Theta - 2}.$$

As a result, we obtain that,

$$\text{for } -1 < \sigma_{\text{so}} < 4 - \eta, \quad \Theta = \frac{2}{\sigma_{\text{so}} + 4}. \tag{31}$$

Equation (31) is valid when large scales are permanent, i.e., when $\sigma_{\text{so}} < 4 - \eta$. An important question is whether this prediction can be extended beyond this condition. For $\sigma_{\text{so}} > 4$, we note that the infrared exponent of $\mathbb{Q}^{\text{so}}$ is not constant and eventually tends to 4. Thus, to answer our question, we only need to consider what happens when σ_{so} is in the interval $[4 - \eta, 4]$. In this interval, the permanence of large eddies is not necessarily verified and we cannot derive a strict relation linking $\mathbb{Q}^{\text{so}}$ to σ_{so}. However, by analogy with the results obtained in homogeneous turbulence, we may expect that Eq. (31) will still provide a reasonable estimate of Θ. Moreover, we may expect that corrections similar to the ones introduced in Refs. [23,24,33–35] can be brought to Eq. (31) to account for the influence of backscattering transfer terms. The simplest of these corrections consists in limiting the value of Θ to the value it reaches for $\sigma_{\text{so}} = 4 - \eta$ [23,24,34]. Knowing that for $\sigma_{\text{so}} > 4$ the infrared exponent of $\mathbb{Q}^{\text{so}}$ reverts to 4, this limit value will be reached not only for $4 - \eta \leqslant \sigma_{\text{so}} \leqslant 4$ but also for $\sigma_{\text{so}} > 4$.

Then, using this particular correction, the following extension of Eq. (31) can be proposed:

$$\text{for } \sigma_{\text{so}} > -1, \quad \Theta = \frac{2}{\min(\sigma_{\text{so}}, 4 - \eta) + 4} \geqslant \frac{2}{\min(\sigma_{\text{so}}, 4) + 4}. \tag{32}$$

This formula is identical to Eq. (31) for $\sigma_{\text{so}} < 4 - \eta$ and predicts that Θ saturates to a minimum value:

$$\Theta_{\min} = \frac{1}{4 - \eta/2} \quad \text{for } \sigma_{\text{so}} \geqslant 4 - \eta.$$

If η is on the order of 0.5 as in homogeneous turbulence, then this minimum value is on the order of

$$\Theta_{\min} \approx 0.27 \quad \text{for } \sigma_{\text{so}} \geqslant 3.5.$$

Note that in our previous study on small Atwood number Richtmyer–Meshkov turbulence [15], η was denoted by ϵ. It was found to be close to 0 and a value $\Theta_{\min} \approx 0.25$ for $\sigma_{\text{so}} \geqslant 4$ was found to be in good agreement with simulations. However, given the uncertainty surrounding the numerical evaluation of Θ, it is not evident that the simulations of Ref. [15] were sufficient to discriminate between the two values of $\Theta_{\min}$ and η.

B. Comparison with the small Atwood number regime

Equation (32) can be compared to the value of Θ derived in the Boussinesq limit in our previous work [15]. In Ref. [15], the expression of Θ is formally identical to Eq. (32) except for one important aspect: Θ is parameterized by the infrared exponent σ_{vel} of the velocity spectrum and not by σ_{so}.

In the Boussinesq limit, the velocity and solenoidal momentum spectra are identical so that σ_{so} and σ_{vel} are equal. Therefore, the predictions of the present work and of Ref. [15] coincide in this particular limit. However, when density variations become strong, the two spectra generally differ and so do their infrared exponents. In general, one has

$$\sigma_{\text{so}} \neq \sigma_{\text{vel}}.$$

As shown in Ref. [24], differences as high as 2 can be observed between the two exponents for high Atwood numbers. As a result, the Boussinesq prediction of Θ, based on the velocity spectrum and on σ_{vel}, cannot be extended straightforwardly to the high Atwood case. The use of the solenoidal momentum spectrum appears to be necessary.

The same comment also applies to the expressions of Θ derived in Refs. [13,14]. These two works predate [24] and constitute the first instances in which the principle of permanence of large eddies has been applied to Richtmyer–Meshkov turbulence. They are also based on the Boussinesq approximation and are formulated by considering the properties of the velocity spectrum. The corresponding values of Θ are then expressed as a function of σ_{vel}, and are identical to the one obtained in Ref. [24]. Their extension to the high-Atwood number case would also require the introduction of the solenoidal momentum s and of its two-point statistics.

C. Comparison with the just-saturated mode and bubble competition theories

Equation (32) of Θ can be reformulated as a function of the infrared exponent m of the initial interfacial perturbation. Given Eq. (30), which connects σ_{so} and m, we can write that,

$$\text{for } m > -2, \quad \Theta = \frac{2}{\min(m, m_{\text{lim}}) + 5}, \quad \text{with} \quad m_{\text{lim}} = 3 - \eta. \tag{33}$$

Notwithstanding the value of m_{lim}, this formula is the one already derived in the just-saturated mode (JSM) theory [8–10,37]. As explained in Ref. [15], this equality is not unexpected. Indeed, the core assumption of the JSM theory is that interfacial perturbations with long wavelengths keep evolving in a linear fashion, even during the self-similar regime. Since the linear growth of the amplitude of a Richtmyer–Meshkov mode is proportional to time, this means that the JSM theory assumes

that the velocity of these large-scale modes is constant in time. In other words, the JSM theory is implicitly built upon the idea that there exists a "modal" velocity spectrum which large-scale content is permanent. This can be seen as another way of formulating the principle of permanence of large eddies which was used in this work and in Refs. [13–15].

A crucial element of Eq. (33) is the presence of a limit exponent m_{lim} with a value slightly below 3. In the present theory, this limit exponent has a well defined origin: it arises because of the existence of a nonlinear backscattering transfer term joining energetic and very large scales. However, in the JSM approach, nonlinear effects are not accounted for and no limit exponent can be inferred from the theory itself. Such an exponent has nonetheless been added heuristically in Ref. [9] with a value close to 3, as in the present work.

As opposed to the JSM approach, the bubble competition theory assumes that the evolution of the mixing zone is entirely driven by nonlinear events. This theory was adapted to the Richtmyer–Meshkov context in Ref. [11]. It predicts a unique value of Θ equal to 0.22. This value can be understood as a prediction for the minimum of Θ reached for $m \geqslant m_{\mathrm{lim}}$ when backscattering transfer terms are dominant. In that case, it would correspond to a value $m_{\mathrm{lim}} \approx 4$ or equivalently to $\sigma_{\mathrm{so}} = 5$. This value is somewhat larger than the exponent $\sigma_{\mathrm{so}} = 4$ associated with backscattering effects in the present work.

D. Comparison with Haan's model

Another prediction for the value of Θ has recently been proposed in Ref. [12]. In this reference, Haan's model [38,39] is used to derive an expression of Θ that turns out to be identical to Eq. (33), except for the value of m_{lim}. In Ref. [12], the following prediction is made:

$$\text{Ref. [12]}: \quad m_{\mathrm{lim}} = 1.$$

This limit exponent corresponds to a minimum value of Θ equal to

$$\text{Ref. [12]}: \quad \Theta_{\mathrm{min}} = 1/3,$$

instead of approximately $1/4$ in the present work. When cast in the theoretical framework of this article, this value would suggest the existence of backscattering processes with an infrared exponent of 2 instead of the value of 4 found in Sec. III. However, as we explain below, this does not appear to be the case.

Haan's model describes the evolution of the amplitudes Z_k of interfacial modes of wavelength $2\pi/k$. To this end, two steps are followed. First, during the linear and weakly nonlinear phases of the instability, the value of Z_k is computed using the linear impulsive model of Richtmyer [1], with the addition of small corrections of order $\mathcal{O}(Z_k^2)$. These corrections are nonlinear and couple the different modes together. In particular, distant interactions are partially accounted for and information can be transferred directly from the peak region of the Z_k spectrum to its small wave number region. This process is akin to the one described in this work and leads to the emergence of a backscattering nonlinear transfer term at small wave number. A first question arises as to whether this backscattering effect is identical to the one predicted in Sec. III. As shown in Appendix D, the answer to this question is no: Haan's model underestimates backscattering phenomena and predicts that they scale as k^6 instead of k^4. This is far from the k^2 scaling that would be required to set $\Theta_{\mathrm{min}} = 1/3$. A reason explaining this difference is the truncation of Haan's expansion to the second order. Even for perturbations with small amplitudes, third order terms are still expected to contribute to the evolution of turbulent spectra on the same level as those retained in Refs. [38,39]. As emphasized in Refs. [40,41], fourth order terms are a combination not only of the product of second-order ones but also of third- and first-order ones. Note also that the truncation to second-order terms is responsible for another unwanted behavior of Haan's model. Because of this truncation, nonlinear transfer terms exhibit an Atwood number dependency such that they simply vanish in the Boussinesq limit. This nonphysical behavior was already noted in Haan's original

article [39] and would disappear if third order terms were accounted for. For the minimum value of Θ, this means that $\Theta_{\min}$ goes from 0 when $\mathtt{A}_t \to 0$ to 1/3 when the Atwood is finite.

Given these different observations, a second question arises concerning the origin of the 1/3 value found in Ref. [12] for Haan's model. As it appears, the 1/3 value is mostly the result of the saturation procedure used in the second step of Haan's model. This second step consists in introducing a saturation amplitude $Z_{\mathrm{sat}}(k)$ beyond which the weakly nonlinear expansion is replaced by a mean field evolution of Z_k, essentially based on dimensional arguments. This saturated evolution does not involve any explicit nonlinear coupling and does not induce any distant interactions *per se*. However, its role is essential for determining how the remaining distant interactions retroact on the whole spectrum and set the value of Θ. In this respect, it should be understood that the weakly nonlinear expansion of Haan is not unique: it is defined up to a $\mathcal{O}(Z_k^3)$ term. The latter is uninmportant in the small Z_k limit but this ceases to be true when Z_k approaches the saturation limit. Thus, several expansions, with distinct properties, are possible. And even though they are all equivalent in the un-saturated regime, each of them can modify the behavior of distant interactions once saturated modes start appearing. Then, depending on the particular and arbitrary choice made for this expansion, different values of Θ can be obtained. An illustration of this property is given in Appendix D. where it is shown that Haan's model can predict minimum values of Θ ranging from 1/4 to 2/3. In Ref. [12], the authors made some choices leading to a value $\Theta_{\min} = 1/3$. But in the end, these choices are arbitrary and so is the value of $\Theta_{\min}$ they obtain.

As a whole, there is a core issue when using Haan's model in saturated/turbulent flows. Indeed, the description of the nonlinear mode coupling in Haan's model is only valid when two conditions are met: when the amplitude of the considered mode Z_k is small and when the main contribution of the mode coupling comes from small amplitude modes. Whenever distant interactions become prevalent, this second condition cannot be verified. In that case, mode coupling is dominated by modes which are larger than the saturation limit and which are by definition not amenable to Haan's analysis. This fundamental discrepancy is not resolved by simply changing the evolution of saturated modes or by suppressing part of their contribution to mode coupling. The action of saturated modes upon small wave numbers should also be modified.

Independently from all these considerations, there is another issue which is specific to the application of Haan's model to Richtmyer–Meshkov turbulence. In Refs. [12,39,42], this particular configuration is treated after the shock crossing, when there is no more acceleration. By doing so, part of the nonlinear terms which have been generated by the impulsive acceleration are unfortunately discarded. The missing terms are necessary to obtain correct infrared exponents just after the shock passage (see Appendix D). This can however be easily corrected.

VI. VALIDATION

A. Description of the simulations

To validate the results derived in the previous sections, we perform several implicit large eddy simulations (ILES) with the massively parallel code TRICLADE [43]. The compressible mutimaterial Euler equations are solved without physical viscosity or diffusivity, with a shock capturing scheme providing just enough numerical viscosity and diffusivity to ensure stability. No explicit LES subgrid model is added. More precisely, for this work, the MUSCL-based finite volume Godunov method referred to as M5 in Ref. [43] is used. It is accurate to fifth order in space and is combined with a low-storage strong stability preserving Runge-Kutta scheme of third-order time accuracy. Primitive variables are reconstructed with a monotonicity-preserving (MP) limiter [44]. A Harten-Lax-van Leer-Contact (HLLC) numerical flux [45] is used at each cell face.

The simulations are performed with the methodology introduced in Ref. [46] for the Θ-group study. At initial time, the domain is divided into three subdomains along the x_3 axis. The interval $x_3 < x_{\mathrm{shock}}$ corresponds to shocked heavy fluid, the interval $x_{\mathrm{shock}} < x_3 < x_{\mathrm{interf.}} + h(\boldsymbol{x}_\perp)$ to un-shocked heavy fluid, and the interval $x_3 > x_{\mathrm{interf.}} + h(\boldsymbol{x}_\perp)$ to unshocked light fluid. The shock has

TABLE I. Main simulation parameters.

Atwood number	Shock Mach number	Grid resolution	Domain size	Interface position	Shock position
$A_t = 0.67$	$M_S = 1.1$	$N_p = 512$	$L_{dom} = 2\pi$	$x_{interf.} = 0$	$x_{shock} = -0.1L_{dom}$

a Mach number M_S and induces a velocity jump ΔU. The gas interface is given an initial velocity such that, after the shock passage, its mean position is approximately at rest.

This initial configuration is set-up in a domain of size $L_{dom} \times L_{dom} \times 2.5L_{dom}$ and is discretized by a grid with $N_p \times N_p \times 2.5N_p$ cells. The grid size is consequently regular and equal to: $\Delta x = L_{dom}/N_P$. The initial position of the interface is set at $x_{interf.} = 0$ and the initial position of the shock is $x_{shock} = -0.1L_{dom}$. Table I summarizes the main parameters of the simulations. A small shock Mach number has been retained in agreement with one of the main assumption of this study. By contrast, the Atwood number has been set to a high value, corresponding to a ratio between the heavy and light fluid densities of about 5.

As in the preceding sections, $h(\boldsymbol{x}_\perp)$ defines the height of a small perturbation around the interface. It has a zero-mean $\overline{h} = 0$, a root-mean square (RMS) value $\sqrt{\overline{h^2}}$ and a power spectrum $P_h(k_\perp)$. The latter is initialized with the following expression:

$$P_h(k_\perp) = \overline{h^2} k_0^{-1} \frac{2^{(m+3)/2}}{\Gamma(\frac{m+1}{2})} \left(\frac{k_\perp}{k_0}\right)^m e^{-2(k_\perp/k_0)^2}, \tag{34}$$

where m is the infrared exponent of P_h and k_0 is the approximate peak wave number of the spectrum. The corresponding peak wavelength is $\lambda_0 = 2\pi/k_0$. The parameters defining this spectrum are given in Table II. As can be seen from this table, five simulations are performed, each with a different value of the infrared exponent m.

Starting from these initial conditions, the simulations are led in two steps. First, the shock propagates, crosses the interface and travels until it almost reaches the end of the domain. Then, the simulation is stopped. The central part of the domain, from $x_3 = -L_{dom}/2$ to $x_3 = L_{dom}/2$, is extracted and left as is, while in the two subdomains $|x_3| > L_{dom}/2$ the density, velocity and pressure fields are replaced by uniform values. This modified state is then used to initialize a second simulation which is run until the size of the mixing zone reaches about $1/3$ of L_{dom}. This procedure, which has been devised in Ref. [46], allows to avoid dealing with the interaction between the shock and the outlet boundary condition. Such interactions usually lead to the generation of spurious waves that prevent observing a clear evolution of the mixing zone.

Note that the shock/interface interaction occurs approximately at

$$t_c \approx 0.03 \, t_{ref},$$

where t_{ref} is a reference timescale defined by

$$t_{ref} = \frac{\lambda_0^2}{\sqrt{\overline{h^2}} A_t \Delta U}. \tag{35}$$

As for the beginning of the second step, it occurs approximately at time

$$t \approx 0.08 \, t_{ref}.$$

TABLE II. Parameters of the interface deformation.

RMS height	Peak wavelength	Infrared exponent
$\sqrt{\overline{h^2}} = 2.5\Delta x$	$\lambda_0 = \frac{2\pi}{k_0} = 20\Delta x$	$m \in \{0, 1, 2, 3, 5\}$

(a) Iso-concentrations and velocity spectrum at $t/t_{\rm ref} = 0.06$

(b) Iso-concentrations and velocity spectrum at $t/t_{\rm ref} \approx 0.3$

(c) Iso-concentrations and velocity spectrum at $t/t_{\rm ref} \approx 25$
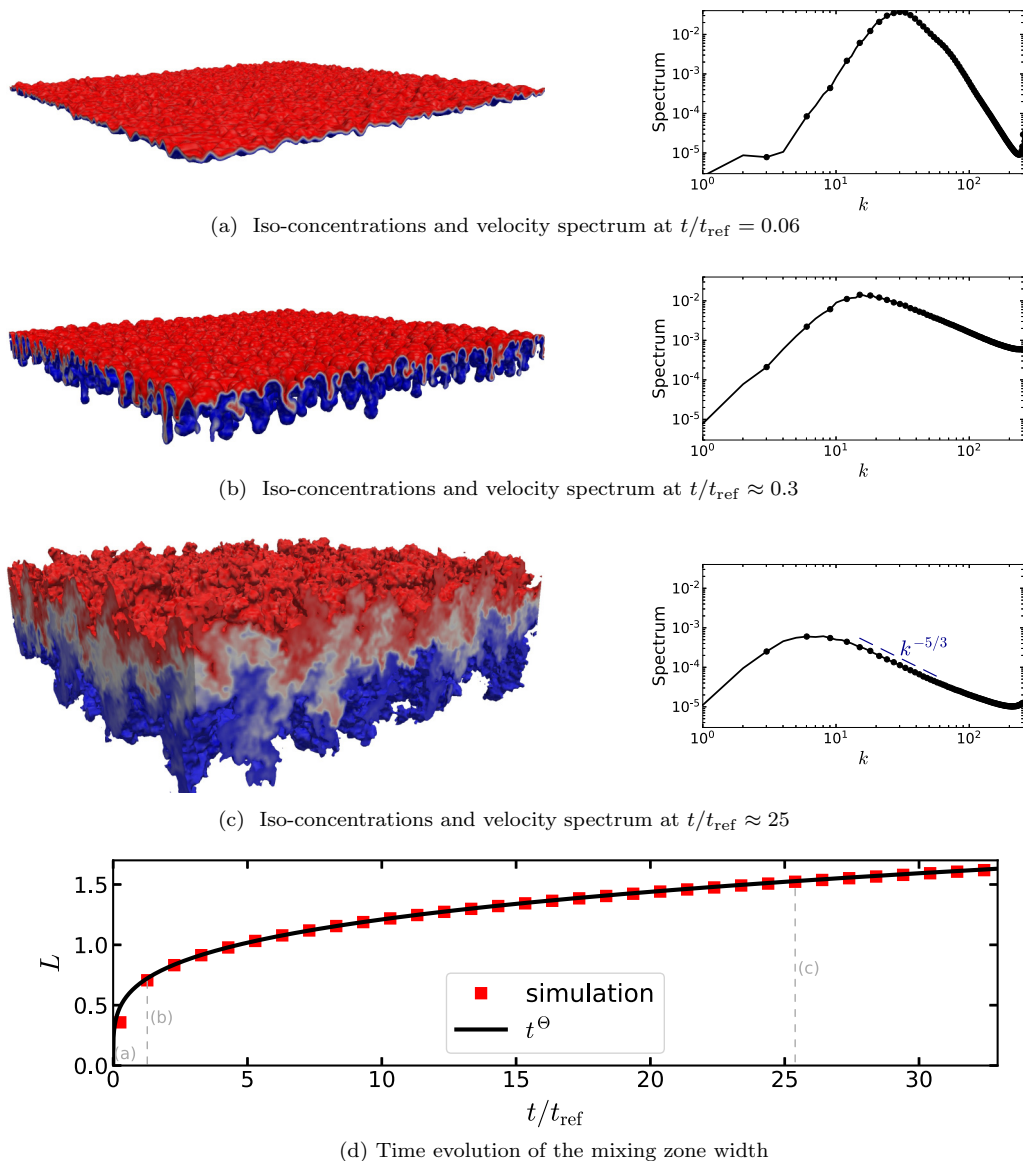

(d) Time evolution of the mixing zone width

FIG. 3. Illustration of the evolution of the simulation with $m = 5$ ($\sigma_{\rm so} = 6$). Panels (a–c), left column: isosurfaces of the concentration field at different times. The concentration levels are varied between 0.1 in blue (light fluid) and 0.9 in red (heavy fluid). The shock propagates from the bottom towards the top of each image. Panels (a–c), right column: velocity spectrum at different times. A $k^{-5/3}$ fiducial is plotted in panel (c). Given the resolution of the simulation, this is only meant as an indication. Panel (d): Evolution of the mixing zone width and comparison against a power law. The times at which the iso-concentrations and spectra are plotted in panels (a–c) are shown in gray.

B. Typical evolution of a simulation

The evolutions of the simulations described above share several common points. To illustrate these similarities, we focus on the simulation performed with $m = 5$ and we display in Fig. 3 several pieces of information related to it. First of all, in the left column of Figs. 3(a)– 3(c), snapshots of the

(a) Time evolution of the peak values of $\overline{s_i' s_i'}$ and $\overline{\rho}^2 \overline{u_i' u_i'}$ (b) Time evolution of the profile widths of $\overline{s_i' s_i'}$ and $\overline{\rho}^2 \overline{u_i' u_i'}$
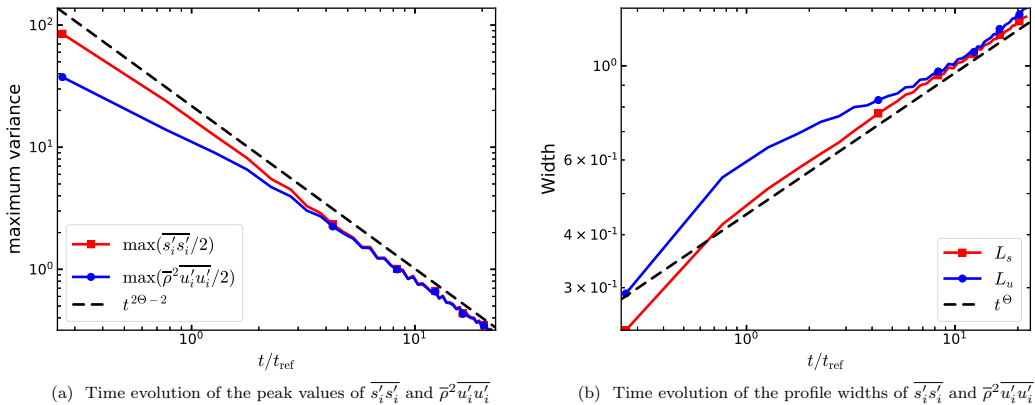
FIG. 4. Comparison between the evolutions of the variances of the solenoidal momentum and of the velocity field for the simulation with $m = 1$ ($\sigma_{\text{so}} = 2$). The fiducial curves appearing with dashed lines in the two subfigures are plotted with $\Theta = 1/3$.

isosurfaces of the concentration field are shown at different times. For the earliest time, the shock has just crossed the interface and the flow can be thought to still be in its linear phase. The amplitude of the perturbation remains small with respect to its discernible wavelength. For the second one [Fig. 3(b)], the flow has reached a nonlinear stage. Structures looking like spikes at the bottom and bubbles at the top can be clearly distinguished. Besides, a strong asymmetry between the heavy and light fluids can be noted, as expected from the high density contrast of the simulation. Finally, the last snapshot [Fig. 3(c)] corresponds to a time where the flow is already tending towards its self-similar turbulent asymptotic state.

On the right side of these snapshots, the spectrum of the velocity field is shown. One can observe a transition from a spectrum peaked at high wave numbers around $k \approx k_0$ [Fig. 3(a)] to a spectrum peaked at smaller and smaller wave numbers [Fig. 3(c)]. This corresponds to the appearance of larger and larger turbulent structures. Besides, one can also notice that the peak value of the spectrum is decreasing. The flow and its kinetic energy are indeed decaying.

The last information shown in Fig. 3 is the evolution of the mixing zone width. The latter is computed as

$$L = 6 \int \overline{c}(1 - \overline{c}) dx_3. \tag{36}$$

In Fig. 3(d), one can observe that after a short transient, the simulation approaches a state where L obeys an approximate power law. An exponent $\Theta \approx 0.25$ appears to offer a good fit. The value of this exponent for the $m = 5$ simulation and the other ones will be discussed further in Sec. VI F.

Since our analysis is based on the properties of the solenoidal momentum s, it is interesting to illustrate the typical behavior of its variance $\overline{s_i' s_i'}$. To this end, we now focus on the simulation performed with $m = 1$ and show in Fig. 4(a) the decay of the peak value of $\overline{s_i' s_i'}$. It can be seen that this peak value decreases approximately as a power law and that the corresponding decay exponent is close to $2\Theta - 2$ with $\Theta \approx 1/3$. The latter value is the one expected from Eq. (32). Figure 4(a) also compares the decay of $\overline{s_i' s_i'}$ against that of $\overline{\rho}^2 \overline{u_i' u_i'}$. The peak values of the two quantities display significant discrepancies at the start of the flow evolution but end up being very close for t larger than a few t_{ref}. One also notes that $\overline{s_i' s_i'}$ appears to reach its self-similar evolution earlier than $\overline{\rho}^2 \overline{u_i' u_i'}$.

These general remarks can also be extended to Fig. 4(b). This figure compares the widths of the profiles of $\overline{s_i' s_i'}$ and $\overline{\rho}^2 \overline{u_i' u_i'}$ for the simulation with $m = 1$. These widths are defined
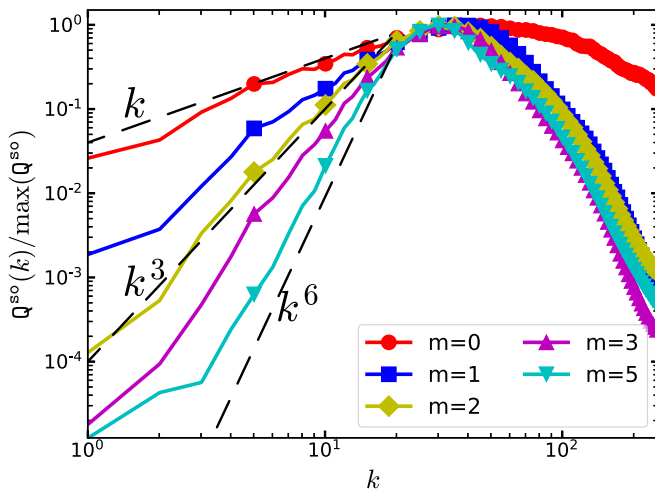
FIG. 5. Spectrum of the solenoidal component of the momentum at time $t/t_{\mathrm{ref}} = 0.06$, just after the shock passage.

as

$$L_s = \frac{\int \overline{s_i' s_i'} dx_3}{\max_{x_3}(\overline{s_i' s_i'})} \quad \text{and} \quad L_u = \frac{\int \overline{\rho}^2 \overline{u_i' u_i'} dx_3}{\max_{x_3}(\overline{\rho}^2 \overline{u_i' u_i'})}.$$

These two quantities tend to a power-law evolution at large time, with an exponent Θ close to $1/3$. Besides, after a few t_{ref}, their values become close to one another, even though some differences exist at initial time. While not displayed here, similar observations also apply to the other simulations performed with different values of m.

Hence, even though their transients are different, one may expect that $\overline{s_i' s_i'}$ and $\overline{\rho}^2 \overline{u_i' u_i'}$, or more simply $\overline{u_i' u_i'}$, give access to comparable information concerning the self-similar state of the flow. In this regard, the value of the self-similar exponent Θ will be discussed by looking at the decay of $\overline{u_i' u_i'}$ and not $\overline{s_i' s_i'}$ in Sec. VI F. This choice has been made because $\overline{u_i' u_i'}$ is a quantity readily available in most simulation codes. This opens a possibility for cross validations that would be more difficult to perform with $\overline{s_i' s_i'}$.

C. Initial conditions

Equation (30) of Sec. IV states that the post-shock infrared exponent σ_{so} of $\mathtt{Q}^{\mathrm{so}}$ is directly related to the infrared exponent m of the height spectrum P_h [here defined by Eq. (34)]. To verify this prediction, we plot in Fig. 5 the value of $\mathtt{Q}^{\mathrm{so}}$ at time $t/t_{\mathrm{ref}} = 0.06$, shortly after the shock passage. It can be seen that the exponent σ_{so} is indeed equal to $m + 1$ and that for our five simulations performed with $m \in \{0, 1, 2, 3, 5\}$, its values are

$$\sigma_{\mathrm{so}} \in \{1, 2, 3, 4, 6\}.$$

For $m = 5$, one can see a slight deviation from $\sigma_{\mathrm{so}} = 6$ for the smallest wave numbers. This is expected since, as shown in Appendix B, a k^4 scaling will eventually overtake this k^6 component when $k \to 0$.

D. Nonlinear transfer term

A crucial prediction made in Sec. III concerns the scaling of the nonlinear transfer term $\mathtt{T}$ of $\mathtt{Q}^{\mathrm{so}}$ appearing in Eq. (14); following Eq. (15), the predominance of distant interactions is such that $\mathtt{T}$
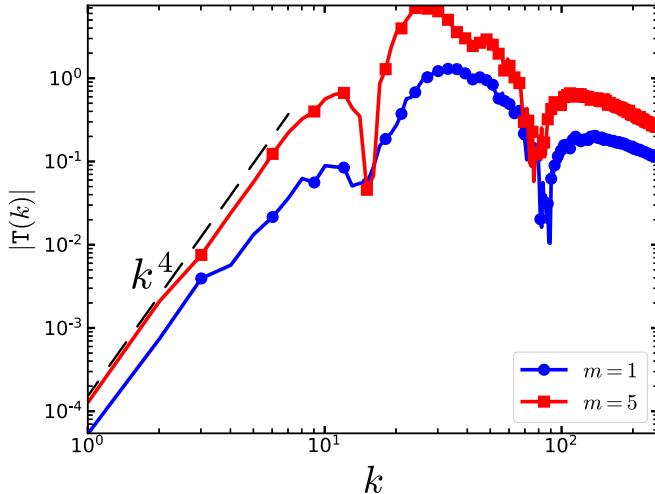
FIG. 6. Absolute value of the transfer term of the solenoidal momentum spectrum at time $t/t_{\mathrm{ref}} = 0.26$ for $m = 1$ and $m = 5$ ($\sigma_{\mathrm{so}} = 2$ and $\sigma_{\mathrm{so}} = 6$).

scales as k^4 for $\sigma_{\mathrm{so}} \geqslant 2$. To verify this prediction, the absolute value of $\mathtt{T}$ is displayed in Fig. 6 for the simulations $m = 1$ and $m = 5$ ($\sigma_{\mathrm{so}} = 2$ and $\sigma_{\mathrm{so}} = 6$) at time $t = 0.26 \, t_{\mathrm{ref}}$. A k^4 scaling can be clearly observed at small wave numbers, as expected from the theory.

We recall that the infrared exponent of $\mathtt{T}$ eventually sets the minimum value of Θ when large eddies are permanent. The observed k^4 scaling is associated with a minimum value close to $1/(4 - \eta/2)$. By contrast, to obtain a minimum value equal to $1/3$, $\mathtt{T}$ would have to scale as k^2. Such an infrared scaling is clearly not observed in our simulations. A further and more direct appraisal of the value of Θ is given in Sec. VI F.
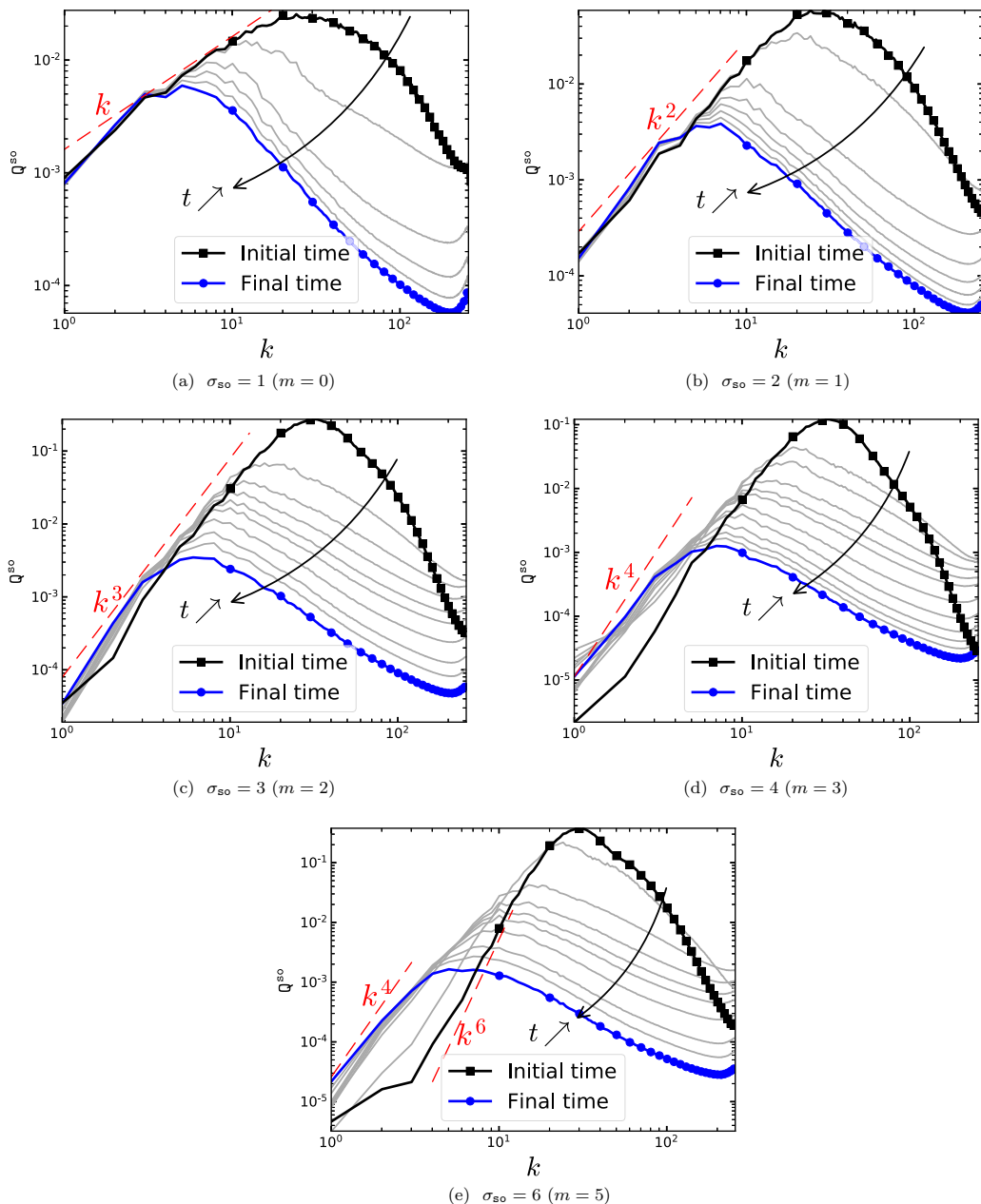
E. Permanence of large eddies

The core result of this work, deduced from the assumptions derived in Sec. III, deals with the permanence of large eddies. For the solenoidal momentum spectrum, large-scale initial conditions are predicted to be preserved at all times when the infrared exponent verifies $s_0 < 4 - \eta$, with η a parameter expected to be on the order of 0.5. Figure 7 shows $\mathtt{Q}^{\mathrm{so}}$ at different times and for different σ_{so}. It can be seen that for $\sigma_{\mathrm{so}} \lesssim 3$, $\mathtt{Q}^{\mathrm{so}}$ remains constant at small wave numbers. For $\sigma_{\mathrm{so}} = 3$, a small departure from initial conditions is already observed. For $\sigma_{\mathrm{so}} = 4$, the infrared exponent remains constant but the prefactor of the infrared power law displays a significant evolution in time. Finally, for $\sigma_{\mathrm{so}} = 6$, the initial scaling of the spectrum is not preserved. Instead, it is replaced by a k^4 scaling. All these observations are coherent with the principle of permanence of large eddies as expressed at the end of Sec. III.

Besides, to illustrate that this principle applies to $\mathtt{Q}^{\mathrm{so}}$ and not to the velocity spectrum $\mathtt{E}$, traditionally used in constant density flows, we plot in Fig. 8 the value of $\mathtt{E}$ at different times for $\sigma_{\mathrm{so}} = 2$. As can be seen, the initial condition of $\mathtt{E}$ is not preserved at large scales despite scaling as k^2. This behavior must be contrasted with the one observed for $\mathtt{Q}^{\mathrm{so}}$ in Fig. 7(b).

F. Value of Θ

To conclude this validation, we now turn our attention to the value of Θ. In Sec. V, we argued that, whenever large eddies are permanent, the value of Θ is set by the infrared slope σ_{so} of the solenoidal momentum spectrum. Besides, we also argued that Θ should reach a minimum value

(a) $\sigma_{\mathrm{so}} = 1$ $(m = 0)$

(b) $\sigma_{\mathrm{so}} = 2$ $(m = 1)$

(c) $\sigma_{\mathrm{so}} = 3$ $(m = 2)$

(d) $\sigma_{\mathrm{so}} = 4$ $(m = 3)$

(e) $\sigma_{\mathrm{so}} = 6$ $(m = 5)$

FIG. 7. Evolution of the solenoidal momentum spectrum for different σ_{so}.

close to $1/(4 - \eta/2)$ and set by the infrared exponent of the nonlinear transfer term. These two predictions are summed up in Eq. (32).

To check these predictions, we compute two instantaneous estimators of the value of Θ. The first one, $\Theta_{\mathrm{simu}}^{(1)}$, is based on the concentration field. More precisely, it measures the growth of the mixing zone width L defined by Eq. (36) [47]. The second, $\Theta_{\mathrm{simu}}^{(2)}$, only involves the fluctuating velocity field and measures the decay of the turbulent kinetic energy $\mathcal{K}$ [48,49]. These two estimators are
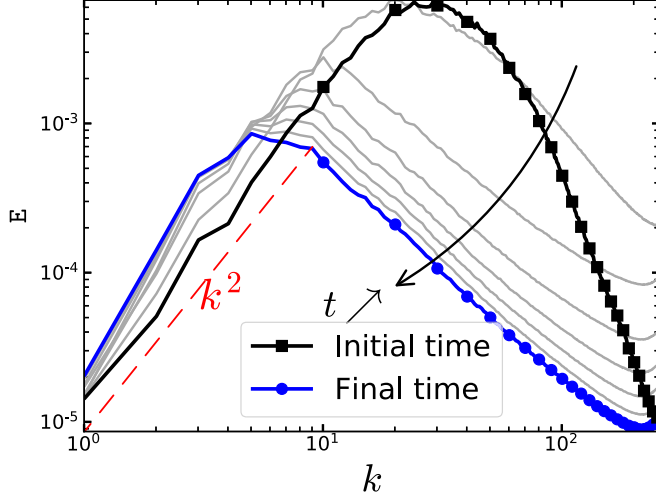
FIG. 8. Evolution of the velocity spectrum for $\sigma_{\mathrm{so}} = 2$ ($m = 1$).

defined as

$$\Theta_{\mathrm{simu}}^{(1)} = \frac{1}{1 + \beta}, \quad \text{with} \quad \beta = -\frac{L\, d_{t^2}^2 L}{(d_t L)^2},$$

$$\text{and} \quad \Theta_{\mathrm{simu}}^{(2)} = \frac{2}{3} + \frac{t}{3} \frac{d_t \mathcal{K}}{\mathcal{K}}, \quad \text{with} \quad \mathcal{K} = \frac{1}{2} \int \overline{u_i' u_i'}\, dx_3.$$

Whenever the flow becomes self-similar, both quantities attain at late times an identical constant value. It should be emphasized that, as opposed to $\Theta^{(1)}$, $\Theta^{(2)}$ is dependent on the value of the virtual time origin of the self-similar regime. This dependency influences the transient value of $\Theta^{(2)}$ but vanishes when time becomes much larger that the absolute value of this time origin. This information should be kept in mind when interpreting $\Theta^{(2)}$ since a precise estimate of the time origin is not available.

The evolutions of $\Theta_{\mathrm{simu}}^{(1)}$ and $\Theta_{\mathrm{simu}}^{(2)}$ are displayed in Fig. 9. For $t \gtrsim 10 t_{\mathrm{ref}}$, plateaus with slow variations can be observed for the different simulations. This suggests that a self-similar regime is approximately reached after this time. It can be seen that the extent of these plateaus is shorter for

(a) Time evolution of $\Theta_{\mathrm{simu}}^{(1)}$

(b) Time evolution of $\Theta_{\mathrm{simu}}^{(2)}$
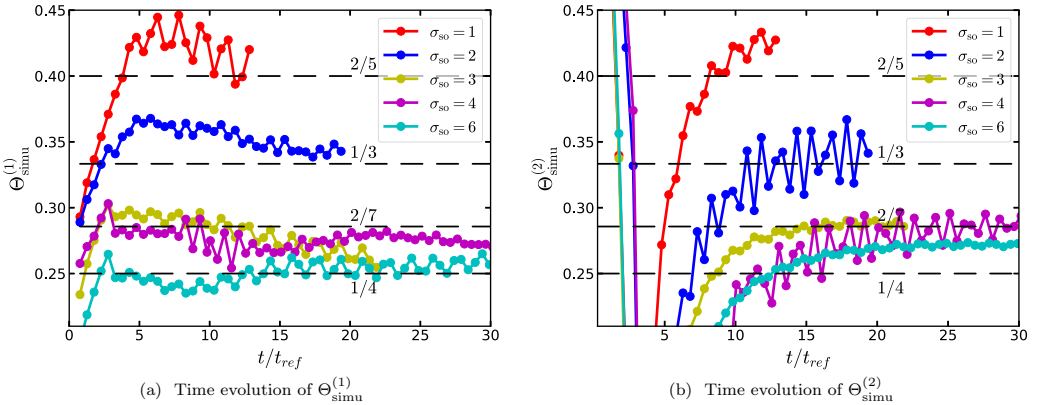
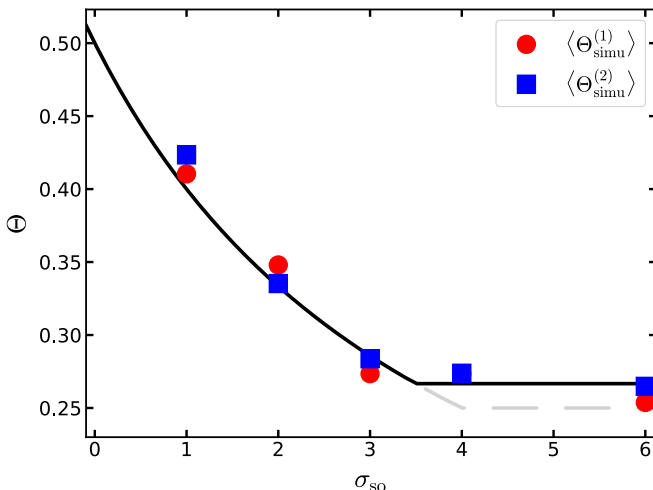FIG. 9. Instantaneous measures of the growth exponent Θ.

FIG. 10. Comparison between the averaged measures of Θ (symbols) and Eq. (32) with $\eta = 0.5$ (black thick line). The prediction obtained with $\eta = 0$ is also shown with a gray dashed line.

smaller values of σ_{so}. Indeed, for simulations with smaller σ_{so}, the size of the mixing zone grows faster and reaches a $1/3$ of L_{dom} earlier. The latter criterion defines the time when simulations are stopped to avoid confinement effects. It can also be noted that the plateau values of $\Theta_{simu}^{(1)}$ and $\Theta_{simu}^{(2)}$ are similar. This indicates that the self-similar properties of the concentration and velocity fields are compatible with one another. Moreover, while not displayed here, we checked that estimates of Θ based on the solenoidal momentum are also coherent with $\Theta_{simu}^{(1)}$ and $\Theta_{simu}^{(2)}$ [see Figs. 4(a) and 4(b)].

The averaged value of the different plateaus is denoted by $\langle \Theta_{simu}^{(i)} \rangle$ for $i = 1, 2$ and is computed as

$$\langle \Theta_{simu}^{(i)} \rangle = \frac{\int_{t_1}^{t_2} \Theta_{simu}^{(i)}(u)\,du}{t_2 - t_1},$$

with $t_1 = 10 t_{ref}$ and t_2 the end time of the simulation This time average is compared against the prediction of Θ given by Eq. (32) in Fig. 10. A satisfactory agreement is observed. In particular, for $\sigma_{so} \geqslant 4$, the value of Θ measured in simulations appears to be close to $1/(4 - \eta/2)$ with $\eta = 0.5$. This value is coherent with the infrared exponent $\sigma_{so} = 4$ of the nonlinear backscattering term observed in figure 6.

VII. CONCLUSIONS

In this work, we studied the large-scale structure of Richtmyer–Meshkov turbulent mixing zones with large density contrasts and small turbulent Mach numbers. Following prior results [24], we focused on the spectrum $\mathbb{Q}^{so}$ of the solenoidal component of the momentum. As in decaying homogeneous turbulence, we showed that a principle of permanence of large eddies can be expressed in terms of this spectrum: whenever the infrared exponent σ_{so} of $\mathbb{Q}^{so}$ is smaller than 4, the small wave number content of $\mathbb{Q}^{so}$ remains constant in time. This property allowed us to express the growth rate exponent Θ of the mixing zone as a function of σ_{so}, which is related to the infrared exponent of the initial interfacial perturbation spectrum. For σ_{so} smaller than 4, the formula we obtained is fully equivalent to the one already derived by the just-saturated mode approach [8–10]. For larger σ_{so}, Θ reaches a minimum value close to $1/4$. This minimum is set by the existence of nonlinear backscattering processes dominated by distant interactions. This prediction was compared against existing ones and in particular against the value of $1/3$ recently obtained in Ref. [12]. The origin of

the latter value was traced back to the incomplete way distant interactions are dealt with in saturated mode closures.

To verify the main predictions of this work, we performed implicit large eddy simulations (ILES) of a large Atwood number Richtmyer–Meshkov turbulent mixing zone. The initial conditions of the simulations were varied by changing the infrared exponent of the power spectrum of the initial interface perturbation. The permanence of Q^{so} and the dependency of Θ on σ_{so} were assessed.

As a perspective, this work could be pursued in several directions. For instance, we voluntarily restricted our attention to initial spectra obeying a power law at large scales. Additional shapes of the initial spectrum could be studied. A first step in this direction has been taken in Appendix C. Besides, we also restricted this study to weak shocks. An extension to moderate shocks could be envisioned by determining the amount of solenoidal momentum deposited in the bulk by the transmitted shock relaxation.

APPENDIX A: LARGE-SCALE EVOLUTION OF THE SOLENOIDAL MOMENTUM SPECTRUM

In this Appendix, we describe the evolution equation of the spectrum Q^{so} of the solenoidal component s of the momentum. Then, we explain how this evolution can be closed at small wave numbers.

1. Evolution of the fluctuating field

The variable-density system Eq. (3) can be decomposed into a mean and fluctuating part. We recall that, for any quantity X, we denote its ensemble mean by $\overline{X}$ and its fluctuation by $X' = X - \overline{X}$. We also recall that the flow is statistically homogeneous and axisymmetric in the directions $\boldsymbol{x}_\perp = (x_1, x_2)$. Within this setting, ensemble means only depend on the inhomogeneous direction x_3, i.e., the direction along which the shock is propagating (see Fig. 1). Then, averaging system Eqs. (3) yields

$$\partial_t \overline{\rho} + \partial_3 \overline{\rho u_3} = \partial_3(\overline{\nu_c \partial_3 \rho}), \tag{A1a}$$

$$\partial_t(\overline{\rho u_3}) + \partial_3(\overline{\rho u_3 u_3}) = -\partial_3(\overline{p} + \overline{\Sigma}_{33}), \tag{A1b}$$

$$\partial_3 \overline{u}_3 = 0. \tag{A1c}$$

Given the homogeneity and axisymmety of the flow in the directions $\boldsymbol{x}_\perp$, one has $\overline{u}_1 = \overline{u}_2 = 0$. Besides, Eq. (A1c) implies that $\overline{u}_3 = 0$, since the velocity field tends to 0 at infinity. Hence, one has

$$\overline{\boldsymbol{u}} = 0. \tag{A2}$$

Subtracting system Eqs. (A1) from system Eqs. (3), we obtain the following evolution for the fluctuating field:

$$\partial_t \rho' + \partial_j(\rho' u_j') = \partial_3 \overline{\rho' u_3'} - u_3' \partial_3 \overline{\rho} + \partial_j(\nu_c \partial_j \rho)', \tag{A3a}$$

$$\partial_t(\rho u_i)' + \partial_j((\rho u_i)' u_j') = \partial_3 \overline{(\rho u_3)' u_3'} - \partial_j(u_j' \overline{\rho u_3} \delta_{i3} + p' \delta_{ij} + \Sigma_{ij}'), \tag{A3b}$$

$$\partial_j u_j' = 0. \tag{A3c}$$

In system Eqs. (A3), we made the unusual choice to work with the fluctuations of the momentum $\rho \boldsymbol{u}$ instead of the Reynolds or Favre fluctuations of the velocity field. The reason is that the momentum—and more precisely its solenoidal part—plays an important role in the analysis of large scales.

2. Evolution of the solenoidal momentum spectrum

We recall that the spectrum of the solenoidal momentum and its modulus are defined by Eqs. (11) and (12). To derive their evolution, we first write the evolution equation for the Fourier transform of

s. This equation is derived directly from the evolution of the Fourier transform of $(\rho u_i)'$. Indeed, in spectral space, both quantities are related by

$$\widehat{s_i'}(\boldsymbol{k}, t) = P_{ij}(\tilde{\boldsymbol{k}})\widehat{(\rho u_j)'}(\boldsymbol{k}, t), \tag{A4}$$

where we recall that $P_{ij}(\tilde{\boldsymbol{k}}) = \delta_{ij} - \tilde{k}_i\tilde{k}_j$ is the projector on incompressible fields and that $\tilde{\boldsymbol{k}} = \boldsymbol{k}/k$ the direction of $\boldsymbol{k}$. Thus, applying the Fourier transform to Eq. (A3b) and multiplying the result by P_{ij}, we obtain that, for $\boldsymbol{k}_\perp = (k_1, k_2) \neq 0$,

$$\partial_t \widehat{s_i'} = -\imath k \mathcal{P}_{ij\cdot k}(\tilde{\boldsymbol{k}})\left(\widehat{(\rho u_j)'u_k'} + \widehat{\rho u_3 u_k'}\delta_{j3} + \widehat{\Sigma_{jk}'}\right), \tag{A5}$$

with the nonsymmetric tensor $\mathcal{P}_{ij\cdot k}(\tilde{\boldsymbol{k}})$ defined by

$$\mathcal{P}_{ij\cdot k}(\tilde{\boldsymbol{k}}) = P_{ij}(\tilde{\boldsymbol{k}})\tilde{k}_k.$$

In the right-hand side of Eq. (A5), one can identify the different source terms of Eq. (A3b), save for one: the pressure gradient which appears in Eq. (A3b) disappears after selecting the solenoidal component of $(\rho u_i)'$. This feature turns out to be crucial for explaining the existence of a large-scale invariant of $\mathcal{Q}^{\text{so}}$ and $\mathtt{Q}^{\text{so}}$.

Starting from Eq. (11), the following evolution of the spectral density $\mathcal{Q}^{\text{so}}$ of the solenoidal momentum s can be derived by

$$\partial_t \mathcal{Q}^{\text{so}}(\boldsymbol{k}, t)\delta(\boldsymbol{k}_\perp - \boldsymbol{k}_\perp') = \overline{\widehat{s_i}(\boldsymbol{k}, t)\partial_t\widehat{s_i}^*(\boldsymbol{k}', t)} + \overline{\partial_t\widehat{s_i}(\boldsymbol{k}, t)\widehat{s_i}^*(\boldsymbol{k}', t)}.$$

Besides, integrating Eq. (A5) in time yields

$$\widehat{s_i}(\boldsymbol{k}, t) = \widehat{s_i}^{(0)}(\boldsymbol{k}) + \int_{t_{\text{qi}}}^t \partial_t\widehat{s_i}(\boldsymbol{k}, t')dt',$$

with $\widehat{s_i}^{(0)}$ the value of $\widehat{s_i}$ at the time $t = t_{\text{qi}}$ marking the beginning of the quasi-incompressible phase. Combining the two equations, we obtain that

$$\partial_t \mathcal{Q}^{\text{so}}(\boldsymbol{k}, t) = 2\mathrm{Re}[\mathcal{T}^{(0)}(\boldsymbol{k}, t)] + 2\int_{t_{\text{qi}}}^t \mathcal{T}(\boldsymbol{k}, t, t')dt',$$

$$\text{with} \quad \mathcal{T}^{(0)}(\boldsymbol{k}, t)\delta(\boldsymbol{k}_\perp - \boldsymbol{k}_\perp') = \overline{\widehat{s_i}^{(0)}(\boldsymbol{k})\partial_t\widehat{s_i}^*(\boldsymbol{k}', t)}$$

$$\text{and} \quad \mathcal{T}(\boldsymbol{k}, t, t')\delta(\boldsymbol{k}_\perp - \boldsymbol{k}_\perp') = \overline{\partial_t\widehat{s_i}(\boldsymbol{k}, t)\partial_t\widehat{s_i}^*(\boldsymbol{k}', t')}. \tag{A6}$$

The component $\mathcal{T}(\boldsymbol{k}, t, t')$ of the transfer term can be expressed further by substituting $\partial_t\widehat{s_i}$ with its value given by Eq. (A5):

$$\mathcal{T}(\boldsymbol{k}, t, t')\delta(\boldsymbol{k}_\perp - \boldsymbol{k}_\perp')$$

$$= k^2 P_{ac}(\tilde{\boldsymbol{k}})\tilde{k}_b\tilde{k}_d\overline{[\widehat{(\rho u_a)'u_b'} + \widehat{\rho u_3 u_b'}\delta_{a3} + \widehat{\Sigma_{ab}'}](\boldsymbol{k}, t)[\widehat{(\rho u_c)'u_d'}^* + \widehat{\rho u_3 u_d'}^*\delta_{c3} + \widehat{\Sigma_{cd}'}^*](\boldsymbol{k}', t')}. \tag{A7}$$

Finally, the evolution of the spectrum $\mathtt{Q}^{\text{so}}$ is obtained by integrating Eq. (A6) over the unit sphere:

$$\partial_t \mathtt{Q}^{\text{so}}(k, t) = \mathtt{T}(k, t), \quad \text{with} \quad \mathtt{T}(k, t) = k^2\oint \mathrm{Re}[\mathcal{T}^{(0)}(\boldsymbol{k}, t)]d\tilde{\boldsymbol{k}} + k^2\int_{t_{\text{qi}}}^t \oint \mathcal{T}(\boldsymbol{k}, t, t')d\tilde{\boldsymbol{k}}\, dt'. \tag{A8}$$

3. Modeling nonlinear interactions at large scales

We denote by $k_{\text{peak}}(t)$ the peak wave number of $\mathtt{Q}^{\text{so}}$ at time t. As in the main text, the expression "small wave number" or "large scales" refers to scales satisfying the condition

$$\text{large-scale range} \quad \equiv \quad k \ll k_{\text{peak}}(t).$$

The large-scale evolution of $\mathbf{Q}^{so}$ is driven by the nonlinear transfer term $\mathbf{T}$ defined by Eq. (A8) and which is the angular integral of $\mathcal{T}^{(0)}$, $\mathcal{T}$. These quantities are not known in terms of second-order spectral correlations and must be modeled.

a. Initial conditions

To begin with, we assume that the initial value $\widehat{\mathbf{s}}^{(0)}$ is uncorrelated with the time derivative of $\widehat{\mathbf{s}}$ at time t. This assumption is of course exact whenever the initial spectrum of $\mathbf{s}$ is null in the range $k \ll k_{\text{peak}}$ and is a good approximation whenever its value is negligible in this range. For more general initial conditions, this assumption can be justified by noting that that the time evolution of $\mathbf{s}$ is linked to the properties of energetic scales $k \sim k_{\text{peak}}(t)$, as will be explained below, and not to scales $k \ll k_{\text{peak}}(t)$. Hence, a decorrelation between $\widehat{\mathbf{s}}^{(0)}$ and $\partial_t \widehat{\mathbf{s}}$ is expected. Thus, we set,

$$\text{for } k \ll k_{\text{peak}}(t), \quad \mathcal{T}^{(0)}(\mathbf{k}, t) = 0.$$

b. Viscous/diffusive effects

Next, we assume that viscous and diffusive effects are negligible at large scales. Consequently, in the expression of $\mathcal{T}$, we neglect all contributions coming from the viscous/diffusive tensor $\widehat{\mathbf{\Sigma}}$. Hence, $\mathcal{T}$ can be simplified as,

$$\text{for } k \ll k_{\text{peak}}(t), \quad \mathcal{T}(\mathbf{k}, t, t')\delta(\mathbf{k}_\perp - \mathbf{k}'_\perp)$$
$$= k^2 P_{ac}(\tilde{\mathbf{k}})\tilde{k}_b\tilde{k}_d \overline{((\widehat{\rho u_a})'u'_b + \widehat{\overline{\rho u_3}u'_b}\delta_{a3})(\mathbf{k}, t)((\widehat{\rho u_c})'u'_d{}^* + \widehat{\overline{\rho u_3}u'_d}{}^*\delta_{c3})(\mathbf{k}', t')}.$$

c. Mean velocity contributions

Compared to the homogeneous case [24], additional correlations appear in the expression of $\mathcal{T}$, those involving the Fourier transform of the mean velocity $\overline{\rho u_3}$ and of the fluctuating velocity. To treat these correlations, we propose a simple closure for $\widehat{\overline{\rho u_3}u'_i}(\mathbf{k}, t)$. To this end, we re-express this term as a function of two-dimensional Fourier transforms:

$$\widehat{\overline{\rho u_3}u'_i}(\mathbf{k}, t) = \frac{1}{2\pi}\int e^{-\imath k_3 x_3}\overline{\rho u_3}(x_3, t)\widehat{u_i'}^{2D}(\mathbf{k}_\perp, x_3, t)dx_3,$$

where $\widehat{u_i'}^{2D}(\mathbf{k}_\perp, x_3, t)$ refers to the 2D Fourier transform of u'_i in the homogeneous directions $\mathbf{x}_\perp = (x_1, x_2)$, at point x_3, at time t and at wave vector $\mathbf{k}_\perp = (k_1, k_2)$. The infinite integral limits of this expression can be exchanged for finite ones. Indeed, $\overline{\mathbf{u}} = 0$, so that we have

$$\overline{\rho u_3} = \overline{\rho}\,\overline{u_3} + \overline{\rho'u'_3} = \overline{\rho'u'_3}.$$

And since the fluctuations of concentration and density are null outside the mixing zone, $\overline{\rho'u'_3}$ is also null in these regions. Thus, we can write that

$$\widehat{\overline{\rho u_3}u'_i}(\mathbf{k}, t) = \frac{1}{2\pi}\int_{-L/2}^{L/2} e^{-\imath k_3 x_3}\overline{\rho'u'_3}(x_3, t)\widehat{u_i'}^{2D}(\mathbf{k}_\perp, x_3, t)dx_3, \tag{A9}$$

making the arbitrary choice that the mixing zone of width L extends from $x_3 = -L/2$ to $x_3 = L/2$.

The next step consists in relating $\widehat{u_i'}^{2D}$ to its 3D counterpart $\widehat{u_i'}$. To this end, we use the fact that the vorticity field is null outside the mixing zone. Then, for $|x_3| > L/2$, one has $\partial_{jj}^2 u'_i = 0$, so that

$$\widehat{u_i'}^{2D}(\mathbf{k}_\perp, x_3, t) = \begin{cases} \widehat{u_i'}^{2D}(\mathbf{k}_\perp, L/2, t)e^{-k_\perp x_3}, & \text{if } x_3 > L/2, \\ \widehat{u_i'}^{2D}(\mathbf{k}_\perp, -L/2, t)e^{k_\perp x_3}, & \text{if } x_3 < -L/2. \end{cases} \tag{A10}$$

We also need to specify the variations of $\widehat{u_i'}^{2D}$ within the mixing zone. Here, we make the assumption that when $k_\perp L \to 0$, $\widehat{u_i'}^{2D}(\mathbf{k}_\perp, x_3)$ varies on a length scale on the order of $k_\perp^{-1}$ in the direction x_3.

This property is verified outside the mixing zone and is extended at its center. Hence, inside the mixing zone, we write the Taylor-expansion,

$$\text{for } -L/2 \leqslant x_3 \leqslant L/2 \quad \text{and} \quad k_\perp L \ll 1, \quad \widehat{u_i'}^{2D}(\boldsymbol{k}_\perp, x_3) = \widehat{u_i'}^{2D}(\boldsymbol{k}_\perp, 0) + \mathcal{O}(k_\perp L). \quad (A11)$$

Combining Eqs. (A10) and (A11) with the definition of the Fourier transform $\widehat{u_i'}(\boldsymbol{k}) = \frac{1}{2\pi} \int e^{-\imath k_3 x_3} \widehat{u_i'}^{2D}(\boldsymbol{k}_\perp, x_3) dx_3$, we obtain that, on first order in kL,

$$\text{for } -L/2 \leqslant x_3 \leqslant L/2 \quad \text{and} \quad kL \ll 1, \quad \widehat{u_i'}^{2D}(\boldsymbol{k}_\perp, x_3, t) = \widehat{u_i'}(k, t) \frac{\pi k^2}{k_\perp}. \quad (A12)$$

The value of $\widehat{u_i'}^{2D}$ outside the mixing zone is obtained by multiplying this expression by $e^{\pm k_\perp x_3}$.

Injecting Eq. (A12) into Eq. (A9) and Taylor-expanding $e^{-\imath k_3 x_3}$ in the limit $|k_3|L \ll 1$, we eventually obtain that

$$\text{for } kL \ll 1, \quad \widehat{\overline{\rho u_3 u_i'}}(\boldsymbol{k}, t) = \frac{k^2 L}{2k_\perp} \langle \overline{\rho' u_3'} \rangle \widehat{u_i'}(\boldsymbol{k}, t), \quad (A13)$$

where $\langle \cdot \rangle$ is the average over the inhomogeneous direction:

$$\langle \cdot \rangle = \frac{1}{L(t)} \int_{-\infty}^{\infty} dx_3. \quad (A14)$$

In the expression for $\mathcal{T}$, $\widehat{\overline{\rho u_3 u_i'}}$ appears with $\tilde{\boldsymbol{k}}$ as a prefactor, in the form $\tilde{k}_b \widehat{\overline{\rho u_3 u_b'}}$. With the proposed closure, this expression becomes

$$\tilde{k}_b \widehat{\overline{\rho u_3 u_b'}} = \frac{k^2 L}{2k_\perp} \langle \overline{\rho' u_3'} \rangle \, \tilde{k}_b \widehat{u_b'} = 0.$$

The last equality comes from the solenoidality of $\boldsymbol{u}'$. To be more accurate, the proposed closure is the leading term of a series of Taylor expansions. The fact that its contribution is equal to zero means that $\tilde{k}_b \widehat{\overline{\rho u_3 u_b'}}$ is determined by the next order terms. But the leading term of $\widehat{\overline{\rho u_3 u_b'}}$, had it not be perpendicular to $\tilde{\boldsymbol{k}}$, is already much smaller than $\widehat{\boldsymbol{u}'}$ and would in any case have given a negligible contribution to $\mathcal{T}$. Hence, there is no need to explicit next order smaller terms that would also be negligible. Therefore, at small wave numbers, the contribution of $\widehat{\overline{\rho u_3 u_b'}}$ to the expression of $\mathcal{T}$ can be neglected. The latter quantity then simplifies as,

$$\text{for } k \ll k_{\text{peak}}(t), \quad \mathcal{T}(\boldsymbol{k}, t, t') \delta(\boldsymbol{k}_\perp - \boldsymbol{k}_\perp') = k^2 \, P_{ac}(\tilde{\boldsymbol{k}}) \tilde{k}_b \tilde{k}_d \overline{\widehat{(\rho u_a)' u_b'}(\boldsymbol{k}, t) \widehat{(\rho u_c)' u_d'}^*(\boldsymbol{k}', t')}.$$

d. Fourth-order correlations

Thus, the transfer term $\mathcal{T}$ depends on a fourth-order two-time correlation involving convolution products between the fluctuations of $\boldsymbol{u}$ and $\rho\boldsymbol{u}$. To model this correlation, we assume that the spectra and cospectra of the fluctuating velocity and momentum $\boldsymbol{u}'$ and $(\rho\boldsymbol{u})'$ peak at a wave number close to $k_{\text{peak}}(t)$. Then, we assume that the largest contribution of a correlation involving $\boldsymbol{u}'$ and $(\rho\boldsymbol{u})'$ comes from a range of wave numbers close to or larger than $k_{\text{peak}}(t)$, while smaller wave numbers only provide a marginal contribution. This energy containing range is denoted by

$$\text{Energy containing range} \equiv k \gtrsim k_{\text{peak}}(t).$$

Even more, we assume that, close to k_{peak}, the amplitudes of the Fourier transforms $\widehat{\boldsymbol{u}'}$ and $\widehat{(\rho\boldsymbol{u})'}$ are much larger than the same amplitudes at $k \ll k_{\text{peak}}$. Note that this assumption cannot be verified if the infrared exponent of the turbulent spectra is equal to or smaller than 2. This limit value corresponds to a spectral density being constant at large scales and is thus not compatible with

the existence of a range containing most of the energy. The subsequent analysis is thus limited to infrared exponents larger than 2.

Applying these assumptions to the fourth-order correlation appearing in the definition of $\mathcal{T}$, we obtain that,

$$
\text{for } k \ll k_{\text{peak}}(t), \; \overline{(\widehat{\rho u_i})'u_j'(\boldsymbol{k}, t)(\widehat{\rho u_k})'u_l'^{*}(\boldsymbol{k}', t')}
$$

$$
= \iint S_{ijkl}(\boldsymbol{p}, \boldsymbol{k}-\boldsymbol{p}, \boldsymbol{q}, \boldsymbol{k}'-\boldsymbol{q}; t, t') d\boldsymbol{p} d\boldsymbol{q} \; \delta(\boldsymbol{k}_\perp - \boldsymbol{k}'_\perp)
$$

$$
\approx \iint_{p \gtrsim k_{\text{peak}}(t), q \gtrsim k_{\text{peak}}(s)} S_{ijkl}(\boldsymbol{p}, \boldsymbol{k}-\boldsymbol{p}, \boldsymbol{q}, \boldsymbol{k}' - \boldsymbol{q}; t, t') d\boldsymbol{p} d\boldsymbol{q} \; \delta(\boldsymbol{k}_\perp - \boldsymbol{k}'_\perp)
$$

$$
\approx \iint_{p \gtrsim k_{\text{peak}}(t), q \gtrsim k_{\text{peak}}(s)} S_{ijkl}(\boldsymbol{p}, -\boldsymbol{p}, \boldsymbol{q}, -\boldsymbol{q}; t, t') d\boldsymbol{p} d\boldsymbol{q} \; \delta(\boldsymbol{k}_\perp - \boldsymbol{k}'_\perp), \tag{A15}
$$

where $S_{ijkl}(\boldsymbol{a}, \boldsymbol{b}, \boldsymbol{c}, \boldsymbol{d}; t, t')\delta(\boldsymbol{a}_\perp + \boldsymbol{b}_\perp - \boldsymbol{c}_\perp - \boldsymbol{d}_\perp) = \overline{(\widehat{\rho u_i})'(\boldsymbol{a}, t)\widehat{u_j'}(\boldsymbol{b}, t)(\widehat{\rho u_k})'^{*}(\boldsymbol{c}, t')\widehat{u_l'}^{*}(\boldsymbol{d}, t')}$. The first equality is the definition of the convolution product. The first approximation is a direct expression of our main assumption and the second one is a Taylor expansion in the limit $k \ll k_{\text{peak}}$. This overall procedure is nothing more than the distant interaction hypothesis usually used to simplify spectral models like the eddy-damped quasinormal model (EDQNM) [22,50].

The end result here is that $\overline{(\widehat{\rho u_i})'u_j'(\boldsymbol{k}, t)(\widehat{\rho u_k})'u_l'^{*}(\boldsymbol{k}', t')}$ only depends on t, t' but not on the wave vector $\boldsymbol{k}$. Thus, the nonlinear transfer term $\mathcal{T}$ can be simplified into the following expression:

$$
\text{for } k \ll k_{\text{peak}}(t), \quad \mathcal{T}(\boldsymbol{k}, t, t') = k^2 \, \mathcal{T}^{\text{dist}}(\tilde{\boldsymbol{k}}, t, t') + \text{H.O.T.}, \tag{A16}
$$

$$
\text{with} \quad \mathcal{T}^{\text{dist}}(\tilde{\boldsymbol{k}}, t, t')\delta(\boldsymbol{k}_\perp - \boldsymbol{k}'_\perp) = k^2 \, P_{ac}(\tilde{\boldsymbol{k}})\tilde{k}_b\tilde{k}_d \; \overline{(\widehat{\rho u_a})'u_b'(\boldsymbol{k}, t)(\widehat{\rho u_c})'u_d'^{*}(\boldsymbol{k}', t')} \bigg|_{p, q \gtrsim k_{\text{peak}}}.
$$

The notation $\overline{\cdot}\,|_{p, q \gtrsim k_{\text{peak}}}$ refers to the restriction of the fourth-order correlations to the energetic range detailed in Eq. (A15). As explained above, this restriction is independent from the wave number $\boldsymbol{k}$, which explains why $\mathcal{T}^{\text{dist}}$ only depends on $\tilde{\boldsymbol{k}}$ and time. The notation H.O.T. is used to denote the next orders of the distant interactions as well as the contribution from local interactions. Note that when the infrared exponent is smaller than 2, these additional terms are not negligible compared to the k^4 contribution. They should in principle be detailed further, for instance by applying a full EDQNM closure to the variable density system. However, this procedure is beyond the scope of this article. Its main outcome would be the occurrence of viscous damping terms (see Refs. [22,50]) that scale as $k^{\sigma_{\text{so}}+2}$ and local terms that scale as $k^{3/2(\sigma_{\text{so}}+1)}$. When $\sigma_{\text{so}} > 2$, these contributions are small compared to the k^4 nonlinear component, as expected from the present analysis. However, when $\sigma_{\text{so}} < 2$, they become dominant. Still, their scaling remains steeper than the initial scaling of $\mathtt{Q}^{\text{so}}$. For this reason, they have a negligible influence over the evolution of $\mathtt{Q}^{\text{so}}$ and need not be detailed in this study.

e. Final model

Combining our different assumptions into Eq. (A8), we eventually obtain the following modeled evolution for $\mathtt{Q}^{\text{so}}$ at large scales,

$$
\text{for } k \ll k_{\text{peak}}(t), \quad \partial_t \mathtt{Q}^{\text{so}}(k, t) = k^4 \, \mathtt{T}^{\text{dist}}(t) + \text{H.O.T.},
$$

$$
\text{with} \quad \mathtt{T}^{\text{dist}}(t) = \int_{t_{\text{qi}}}^{t} \oint \mathcal{T}^{\text{dist}}(\tilde{\boldsymbol{k}}, t, t') d\tilde{\boldsymbol{k}} \, dt'. \tag{A17}
$$

As in homogeneous turbulence, nonlinear interactions possess a component scaling as k^4 at small wave numbers. As already noted in Ref. [24], this classical scaling is a recurrent prediction of turbulence closures in constant density incompressible turbulence, for the nonlinear transfer term of the velocity spectrum. We stress that it applies here to the transfer term of the solenoidal momentum spectrum Q^{so} and not of the velocity spectrum E. Besides, the derivation is done here for an inhomogeneous flow.

APPENDIX B: INTERFACE WITH A GAUSSIAN PERTURBATION

We consider an interface centered around the position $x_3 = 0$ and deformed by a perturbation of height $h(\boldsymbol{x}_\perp)$, with $\boldsymbol{x}_\perp = (x_1, x_2)$ the position in the plane perpendicular to x_3 (see Fig. 1). The perturbation h is assumed to be statistically homogeneous and axisymmetric. We denote by E_h the spectrum of h and by P_h its modulus spectrum:

$$E_h(\boldsymbol{k}_\perp) = \frac{1}{(2\pi)^2} \iint e^{-\imath \boldsymbol{k}_\perp \cdot \boldsymbol{r}_\perp} \overline{h(0) h(\boldsymbol{x}_\perp)} d\boldsymbol{x}_\perp \quad \text{and} \quad P_h(k_\perp) = k_\perp \oint E_h(\boldsymbol{k}_\perp) d\tilde{\boldsymbol{k}}_\perp,$$

with $\boldsymbol{k}_\perp = (k_1, k_2)$ the 2D wave vector in the plane perpendicular to x_3, $k_\perp$ the modulus of $\boldsymbol{k}_\perp$, $\tilde{\boldsymbol{k}}_\perp = \boldsymbol{k}_\perp / k_\perp$ its direction, and $\oint \cdot d\tilde{\boldsymbol{k}}_\perp$ the integration over the unit circle. By definition, the variance σ_h^2 of the perturbation amplitude is given by

$$\sigma_h^2 = \overline{h^2} = \iint E_h(\boldsymbol{k}_\perp) d\boldsymbol{k}_\perp = \int_0^\infty P(k_\perp) dk_\perp.$$

Axisymmetry requires E_h to be isotropic, so that

$$E_h(\boldsymbol{k}_\perp) = E_h(k_\perp) \quad \text{and} \quad P_h(k_\perp) = 2\pi k_\perp E_h(k_\perp).$$

For a nondiffuse interface, a concentration field c equal to 1 when $x_3 > h$ and to 0 when $x_3 < h$ can be defined:

$$c(\boldsymbol{x}) = H[x_3 - h(\boldsymbol{x}_\perp)],$$

with H the Heaviside function. Taking the 3D Fourier transform of this expression and subtracting the mean, we obtain that

$$\widehat{c'}(\boldsymbol{k}) = \frac{1}{(2\pi)^3} \iint e^{-\imath \boldsymbol{k}_\perp \cdot \boldsymbol{x}_\perp} \frac{e^{-\imath k_3 h(\boldsymbol{x}_\perp)} - \overline{e^{-\imath k_3 h(\boldsymbol{x}_\perp)}}}{\imath k_3} d\boldsymbol{x}_\perp.$$

As a result, we deduce that, for $k_\perp \neq 0$, the 3D concentration spectrum $E_{cc}(\boldsymbol{k})\delta(\boldsymbol{k}_\perp - \boldsymbol{k}'_\perp) = \overline{\widehat{c'}(\boldsymbol{k})\widehat{c'}(\boldsymbol{k}')}$ is equal to

$$E_{cc}(\boldsymbol{k}) = \frac{1}{(2\pi)^4} \frac{1}{k_3^2} \iint e^{-\imath \boldsymbol{k}_\perp \cdot \boldsymbol{r}_\perp} (\Psi_{\Delta h}^*(k_3, \boldsymbol{r}_\perp) - |\Psi_h|^2(k_3)) d\boldsymbol{r}_\perp, \tag{B1}$$

with $\Psi_{\Delta h}(k_3, \boldsymbol{r}_\perp) = \overline{e^{ik_3 \Delta h}}$ and $\Psi_h(k_3) = \overline{e^{ik_3 \Delta h}}$ the respective characteristic functions of the two point separation $\Delta h = h(\boldsymbol{r}_\perp) - h(\boldsymbol{0})$ and of the height h. Equation (B1) was already derived in Ref. [15] for $k_\perp \neq 0$ and was shown to be sufficient to determine the main properties of E_{cc} at large scales, without further hypothesis. However, some useful information can be brought forward if we assume that h has Gaussian statistics. In that case, the characteristic functions $\Psi_{\Delta h}$ and Ψ_h are Gaussians and we can write that

$$E_{cc}(\boldsymbol{k}) = \frac{1}{(2\pi)^4} \frac{e^{-k_3^2 \sigma_h^2}}{k_3^2} \iint e^{-\imath \boldsymbol{k}_\perp \cdot \boldsymbol{r}_\perp} \ (e^{k_3^2 \overline{h(\boldsymbol{r}_\perp) h(0)}} - 1) d\boldsymbol{r}_\perp. \tag{B2}$$

Integrating this expression over $\boldsymbol{k}$, we find that

$$\int E_{cc}(\boldsymbol{k}) d\boldsymbol{k} = \frac{1}{2\pi} \frac{\sigma_h}{\sqrt{\pi}}.$$

Since $\int E_{cc}(\boldsymbol{k})d\boldsymbol{k} = \frac{1}{2\pi}\int \overline{c'^2}dx_3$ and since the absence of mixing entails that $\overline{c'^2} = \overline{c}(1 - \overline{c})$, we deduce that, for a Gaussian perturbation, the mixing zone width defined by Eq. (36) is equal to

$$L = 6\int \overline{c}(1-\overline{c})dx_3 = \frac{6}{\sqrt{\pi}}\sigma_h. \tag{B3}$$

This result was derived by other means in Ref. [46].

Since we are studying large scales, we are not interested in expressing the properties of $E_{cc}(\boldsymbol{k})$ at all wave numbers, but only at small ones. Thus, we aim to simplify Eq. (B2) in the limit $k\sigma_h \ll 1$, i.e., for both $|k_3|\sigma_h \ll 1$ and $k_\perp \sigma_h \ll 1$. In the limit $|k_3|\sigma_h \ll 1$, the Gaussian term in Eq. (B2) can be Taylor expanded. Neglecting terms of order higher than $(k_3\sigma_h)^4$ and using the relation between P_h and $\overline{h(0)h(\boldsymbol{r_\perp})}$, one obtains the following result:

$$\text{For } |k_3|\sigma_h \ll 1, \quad E_{cc}(\boldsymbol{k}) = \frac{1}{(2\pi)^3}\frac{P_h(k_\perp)}{k_\perp}[1 - (k_3\sigma_h)^2] + \frac{k_3^2}{2(2\pi)^4}\iint \frac{P_h(k'_\perp)}{k'_\perp}\frac{P_h(|\boldsymbol{k'_\perp} + \boldsymbol{k_\perp}|)}{|\boldsymbol{k'_\perp} + \boldsymbol{k_\perp}|}d\boldsymbol{k'_\perp}. \tag{B4}$$

To simplify further this expression, we assume that P_h is a peaked spectrum with a maximum located at k_{peak}. The latter is supposed to be at most on the order of $1/\sigma_h$:

$$k_{\text{peak}}\sigma_h \lesssim 1.$$

Then, the convolution product appearing in the previous expression can be Taylor expanded in the limit $k_\perp \sigma_h \ll 1$, in a way reminiscent of the distant interaction approximation used in Sec. III. With this last assumption, we obtain that,

$$\text{for } k\sigma_h \ll 1, \quad (2\pi)^3 E_{cc}(\boldsymbol{k}) = \frac{P_h(k_\perp)}{k_\perp}[1 - (k_3\sigma_h)^2] + A\left(\frac{k_3}{k_{\text{peak}}}\right)^2\sigma_h^2$$

$$\text{with} \quad A = \frac{k_{\text{peak}}^2}{2\sigma_h^2}\int_0^\infty \frac{P_h(\kappa)^2}{\kappa}d\kappa. \tag{B5}$$

The two limits $|k_3|\sigma_h \ll 1$ and $k_\perp \sigma_h \ll 1$ have been combined in the limit $k\sigma_h \ll 1$ which simultaneously imposes both of them. In Ref. [15] and in Sec. IV, only the first term of the right-hand side of Eq. (B5) is accounted for. This term is indeed predominant in the linear limit $k_{\text{peak}}\sigma_h \to 0$ considered in Ref. [15] and in Sec. IV. Nonetheless, it is still interesting to understand how the second term of Eq. (B5) modifies the shape of the concentration spectrum when $k_{\text{peak}}\sigma_h$ is not small.

To this end, let us assume that the spectrum of the interface perturbation is specified at large scales by the power-law Eq. (28) with $C = P_0 k_{\text{peak}}^{-m}$ and $m = s_h - 1$:

$$\text{For } k_\perp \sigma_h \ll 1, \quad P_h(k_\perp) = P_0\left(\frac{k_\perp}{k_{\text{peak}}}\right)^{s_h-1}, \tag{B6}$$

with P_0 a constant and $s_h - 1$ the infrared exponent of P_h.

Before going further, we would like to emphasize that, for $s_h \leqslant 1$, the distant approximation used to derive Eq. (B5) becomes invalid. The spectrum P_h has indeed no maximum at $k = k_{\text{peak}}$ when $s_h \leqslant 1$. As a result, the second-order term of Eq. (B5), the one proportional to A, is not correct any longer. However, the first order of this expression remains accurate and one can still approximate E_{cc} by $P_h(k_\perp)/[(2\pi)^3 k_\perp]$ as done in Ref. [15] and in the main text [Eq. (26)]. As explained in Sec. IV B, this first-order approximation can even be used for negative values of s_h.

This being said, let us assume, in this Appendix, that $s_h > 1$ and that the second-order approximation Eq. (B5) is valid. Then, substituting the power-law expression of P_h into Eq. (B5), and keeping only the main orders, we derive that the modulus concentration spectrum, defined by

$E_{cc} = k^2 \oint E_{cc}(\boldsymbol{k})d\tilde{\boldsymbol{k}}$, is given by,

$$\text{for } k\sigma_h \ll 1, \ (2\pi)^2 E_{cc}(k) = (k/k_{\text{peak}})^{s_h} \, (P_0 k_{\text{peak}}) \, \frac{\sqrt{\pi}\,\Gamma(s_h/2)}{\Gamma((s_h+1)/2)}$$

$$+ (k/k_{\text{peak}})^4 \, \frac{P_0^2 k_{\text{peak}}^4}{3} \int_0^\infty \frac{(P_h(\kappa)/P_0)^2}{\kappa} d\kappa. \tag{B7}$$

When k is infinitely small, the second contribution of the concentration spectrum becomes predominant over the first one whenever $s_h > 4$. However, when k has a small but finite value, this statement must be refined by comparing the orders of magnitude of the two terms on the right-hand side of Eq. (B7). Assuming that $P_0 k_{\text{peak}} \sim \sigma_h^2$, this comparison leads to the definition of the following wave number, for $s_h > 4$:

$$k_{\text{ic}} = k_{\text{peak}}(k_{\text{peak}}\sigma_h)^{2/(s_h-4)}.$$

When $s_h > 4$ and $k_{\text{ic}} \ll k_{\text{peak}}$, two ranges can be observed for $E_{cc}(k)$. In that case, one has

$$E_{cc}(k) \propto \begin{cases} k^{s_h} & \text{for } k_{\text{ic}} \ll k \ll k_{\text{peak}}, \\ k^4 & \text{for } k \ll k_{\text{ic}}. \end{cases} \tag{B8}$$

The value of k_{ic} relative to k_{peak} depends on $k_{\text{peak}}\sigma_h$. When $k_{\text{peak}}\sigma_h \gtrsim 1$, then $k_{\text{ic}} \gtrsim k_{\text{peak}}$ and the intermediate k^{s_h} range will not be observed. By contrast, in the linear limit $k_{\text{peak}}\sigma_h \to 0$, only the intermediate k^{s_h} range will be observed. This linear limit is precisely the one considered in Ref. [15] and Sec. IV and this explains why the k^4 contribution of the concentration spectrum has been left out of the analysis proposed in these two instances.

Another example that is worth mentioning because of its frequent use in simulations is the case when P_h is an annular spectrum, i.e., a spectrum which is null outside of a bounded interval of wave numbers. In that case, P_h vanishes alltogether at small wave numbers and only the second contribution of Eq. (B5) remains. Thus, even though P_h is annular, $E_{cc}(k)$ is not and displays a k^4 scaling at small wave numbers. Besides, the prefactor of this infrared scaling is not universal but depends on several parameters defining the spectrum. To clarify this point, let us consider an annular spectrum of the form

$$\text{Annular spectrum:} \quad \text{If } \ k_{\text{peak}} \leqslant k \leqslant (1+\alpha)k_{\text{peak}}, \text{ then } P_h(k_\perp) = P_0, \quad \text{else} \quad P_h(k_\perp) = 0.$$
$$\tag{B9}$$

Injecting this definition into Eq. (B5), we derive that the modulus concentration spectrum is given by,

$$\text{for } k\sigma_h \ll 1, \quad \frac{E_{cc}(k)}{\int E_{cc}(k)dk/(\alpha k_{\text{peak}})} = (k/k_{\text{peak}})^4 \, \frac{1}{6\sqrt{\pi}} (k_{\text{peak}}\sigma_h)^3 \frac{\ln(1+\alpha)}{\alpha}. \tag{B10}$$

To obtain this formula, we used the relation $\alpha P_0 k_{\text{peak}} = \sigma_h^2$ as well as Eq. (B3). The denominator in the left-hand side gives an estimate of the peak value of $E_{cc}(k)$.

The main conclusion drawn from Eq. (B10) is that annular spectra are not all equivalent as far as large scales are concerned. They all yield a k^4 concentration spectrum but the corresponding prefactor relative to the peak spectrum value varies as a function of two independent parameters: the aspect ratio of the perturbation $k_{\text{peak}}\sigma_h$ and the length of the bounding interval α. What is more, for sufficiently high aspect ratios and sufficiently small bounding intervals, the large-scale range may even provide a nonnegligible contribution to the variance of concentration. As a result, depending on these parameters, two simulations initialized with annular perturbation spectra may yield different flow evolutions. The limit $k_{\text{peak}}\sigma_h \to 0$ is required to guarantee that the large-scale contribution of the concentration spectrum is indeed negligible.
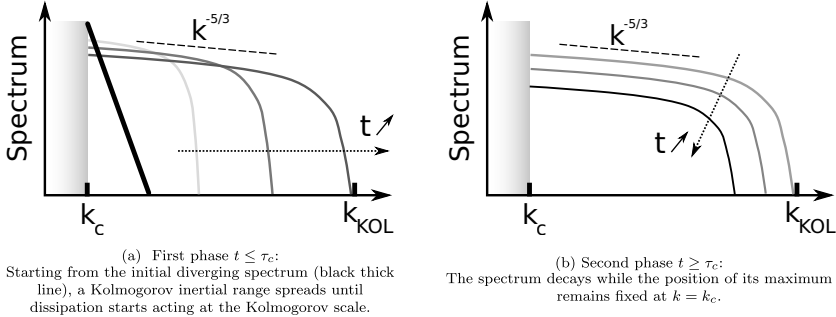
(a) First phase $t \leq \tau_c$:
Starting from the initial diverging spectrum (black thick line), a Kolmogorov inertial range spreads until dissipation starts acting at the Kolmogorov scale.

(b) Second phase $t \geq \tau_c$:
The spectrum decays while the position of its maximum remains fixed at $k = k_c$.

FIG. 11. Schematic representation of the evolution of $\mathbb{Q}^{\mathrm{so}}$ when the initial infrared exponent σ_{so} is smaller than -1. Below the cutoff wave number k_c, turbulent spectra and their transfer terms are null. This "forbidden" zone is represented by the grey area in the two subfigures.

APPENDIX C: FURTHER COMMENTS ON INITIAL CONDITIONS

The purpose of this Appendix is to discuss, in a very qualitative and cursory manner, two issues which have not been dealt with in the main text, but which are sometimes encountered in the literature. First, we would like to give a hint about what occurs when the initial solenoidal momentum spectrum has an infrared exponent smaller than -1. Second, we would like to indicate what may happen when the flow is initialized with a deformation spectrum P_h which is the sum of a power law at large scales and of an annular spectrum at small scales. These two initial conditions are, respectively, depicted in Figs. 11 and 12. We stress that the discussion about these two points is not supported by any simulation or experimental result and remains speculative.

1. Diverging power-law spectrum

In the main text, we restricted our attention to a perturbation height spectrum P_h having an infrared exponent m larger than -2. We now get rid of this limitation and consider that $m < -2$. In that case, the infrared exponent σ_{so} of the solenoidal spectrum $\mathbb{Q}^{\mathrm{so}}$ after the shock crossing is smaller than -1:

$$\sigma_{\mathrm{so}} < -1.$$

With this condition, $\mathbb{Q}^{\mathrm{so}}$ ceases to be integrable when $k \to 0$. To deal with this situation, one has to introduce a cutoff wave number k_c below which all spectra and their transfer terms are null. In practice, k_c corresponds to the size of the simulation domain or to some geometric dimension of the experimental apparatus. The problem is schematized in Fig. 11 and is fully dependent upon the truncating.

(a) $k_{\mathrm{dist}} \ll k_c$

(b) $k_c \ll k_{\mathrm{dist}} \ll k_{\mathrm{peak}}$

(c) $k_{\mathrm{peak}} \ll k_{\mathrm{dist}}$
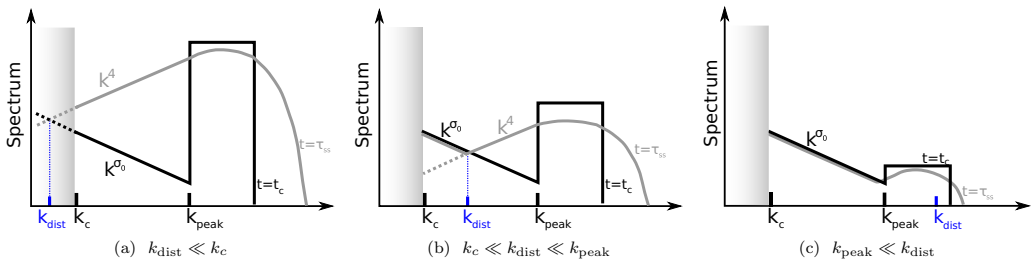
FIG. 12. Schematic representation of the spectrum $\mathbb{Q}^{\mathrm{so}}$ at time t_c, just after shock (black line), and at time τ_{ss}, just after the potential appearance of a large-scale backscattering spectrum (grey line).

The main difference with the situation studied in the main text is that the evolution of the spectrum Q^{so} is now driven by local interactions and, possibly, by distant interactions coming from the range $k \gtrsim k_c$. These interactions are expected to generate a Kolmogorov-like inertial range that will eventually spread from the cutoff wave number k_c to the inverse of the Kolmogorov scale $k_{kol} = \eta_{kol}^{-1}$ [see Fig. 11(a)]. Until this propagation is complete, the dissipation of the kinetic energy can be neglected. Therefore, the total kinetic energy is conserved and, following the arguments of Refs. [51,52], the mixing zone width grows with an exponent equal to

$$\Theta = \tfrac{2}{3}.$$

This exponent may be observed provided the emergence time τ_c of the inertial range is much larger than the characteristic time of the linear growth of the instability τ_{lin}. The maximum value of τ_{lin} is obtained for $k = k_c$ and is equal to

$$\tau_{lin} = \frac{1}{A_t k_c \Delta U}.$$

To estimate the time τ_c, we may simply extrapolate standard results of homogeneous turbulence to the present case [22]. Then, τ_c should be on the order of

$$\tau_c \sim \frac{1}{k_c u'_0},$$

with u'_0 a characteristic scale of the initial velocity field created at the interface. When the turbulent spectra are divergent, the integration of a formula such as Eq. (30) leads to $u'_0 \sim \sqrt{k_c \sigma_h} A_t \Delta U$. As a result, we obtain that

$$\tau_c \sim \frac{1}{k_c \sqrt{k_c \sigma_h} A_t \Delta U} = \frac{\tau_{lin}}{\sqrt{k_c \sigma_h}}.$$

Therefore, in the limit $k_c \sigma_h \to 0$, τ_c is much larger than τ_{lin} and a self-similar regime with $\Theta = 2/3$ can be observed. To sum up, we can write that,

$$\text{for } \sigma_{so} < -1 \quad \text{and} \quad k_c \sigma_h \to 0, \quad \Theta = \tfrac{2}{3}. \tag{C1}$$

This result allows us to generalize Eq. (32) as follows, when $k_c \sigma_h \to 0$:

$$\Theta = \begin{cases} \frac{1}{4 - \eta/2}, & \sigma_{so} > 4 - \eta \\ \frac{2}{\sigma_{so} + 4}, & -1 < \sigma_{so} < 4 - \eta, \\ \frac{2}{3}, & \sigma_{so} < -1 \end{cases} \tag{C2}$$

The first two lines of this equation correspond to Eq. (32), while the last one comes from this Appendix.

If $k_c \sigma_h$ is not infinitely small, then after a finite time τ_c, dissipation starts affecting the flow evolution and a different self-similar regime is expected. More precisely, after $t = \tau_c$, the flow is fully confined [see Fig. 11(b)] and the self-similar regime is dictated by the value of k_c and by the time t. For instance, the turbulent kinetic energy decays as $k_c^{-2} t^{-2}$ and the turbulence concentration flux as $k_c^{-1} t^{-1}$. As for the mixing zone width L, its evolution can be assumed to be driven by the concentration flux so that $\partial_t L \propto k_c^{-1} t^{-1}$. Therefore, we deduce

$$\text{confined regime:} \quad L \sim L_0 \ln(t/t_0),$$

with L_0 and t_0 two unknown constants. Note that this confined regime has been discussed in the case of diverging initial spectra but can also be reached for other types of initial conditions. Note also that a logarithmic growth of the mixing zone width has already been predicted in confined settings using bubble merger models [53] and vortex pair models [54,55]. Finally, it is worth stressing that the study done in the context of homogeneous turbulence in Ref. [56] suggests that the power laws of the confined regime are hard to attain. Several factors detailed in Ref. [56] entail differences with

the expected decay laws. Further information about confinement effects in Richtmyer–Meshkov turbulence can also be found in Ref. [57].

2. Two-range initial spectrum

We now consider an initial deformation of the interface with a spectrum of the form

$$P_h(k_\perp) = \begin{cases} C k_\perp^m, & k_c \leqslant k_\perp \leqslant k_{\text{peak}} \\ P_0/k, & k_{\text{peak}} \leqslant k_\perp \leqslant k_{\text{peak}}(1+\alpha). \\ 0, & \text{elsewhere} \end{cases} \tag{C3}$$

In this equation, C and P_0 are two constants, k_{peak} gives the location of the annular spectrum and α its width, and k_c is a cutoff wave number below which all spectra and their transfer terms are null (see Fig. 12).

After the shock crossing, the solenoidal momentum spectrum Q^{so} can be expressed using Eqs. (25) and (B1). Its shape is more complicated than a mere two-range spectrum. However, it still displays a power law at small wave numbers and a bump centered around the interval $[k_{\text{peak}}, k_{\text{peak}}(1+\alpha)]$. Henceforth, for the sake of simplicity, we choose to approximate Q^{so} at $t = t_c$ by

$$Q^{\text{so}}(k, t_c) = \begin{cases} Q_{\text{ls}} \left(\frac{k}{k_{\text{peak}}} \right)^{\sigma_{\text{so}}}, & k_c \leqslant k \leqslant k_{\text{peak}} \\ Q_{\text{ss}}, & k_{\text{peak}} \leqslant k \leqslant k_{\text{peak}}(1+\alpha), \\ 0, & \text{elsewhere} \end{cases} \tag{C4}$$

where, as before,

$$\sigma_{\text{so}} = m + 1.$$

Within the framework of this analysis, the two constants Q_{ls} and Q_{ss} need not be precisely defined. Only their order of magnitude is of interest. The latter can be estimated by assuming that Q^{so} is on the order of $k^2 Q^{\text{so}}$ taken at the angle $\theta = \pi/2$. Then, according to Eqs. (B4) and (25), one deduces that

$$Q_{\text{ls}} \sim (\mathcal{C} \Delta \rho^+ \Delta U)^2 C k_{\text{peak}}^{\sigma_{\text{so}}} \quad \text{and} \quad Q_{\text{ss}} \sim (\mathcal{C} \Delta \rho^+ \Delta U)^2 P_0.$$

These estimates can be rewritten using the perturbation height variances σ_{ls}^2 and σ_{ss}^2 contained, respectively, by large and small scales:

$$\sigma_{\text{ls}}^2 = \int_{k_c}^{k_{\text{peak}}} P_h(k_\perp) dk_\perp \quad \text{and} \quad \sigma_{\text{ss}}^2 = \int_{k_{\text{peak}}}^{k_{\text{peak}}(1+\alpha)} P_h(k_\perp) dk_\perp.$$

One obtains that

$$Q_{\text{ls}} \sim (\mathcal{C} \Delta \rho^+ \Delta U)^2 \frac{\sigma_{\text{ls}}^2}{A} \quad \text{and} \quad Q_{\text{ss}} \sim (\mathcal{C} \Delta \rho^+ \Delta U)^2 \frac{\sigma_{\text{ss}}^2}{\ln(1+\alpha)}, \tag{C5}$$

with $A = \frac{1}{\sigma_{\text{so}}}[1 - (\frac{k_c}{k_{\text{peak}}})^{\sigma_{\text{so}}}]$ if $\sigma_{\text{so}} \neq 0$, and $A = \ln(k_{\text{peak}}/k_c)$ if $\sigma_{\text{so}} = 0$.

Following Eq. (15), the small-scale annular component of the spectrum generates distant interactions which are responsible for a backscattering transfer term T_{ss} scaling as k^4 at small wave numbers:

$$\text{For } k \ll k_{\text{peak}}, \quad T_{\text{ss}} = k^4 \, T_{\text{ss}}^{\text{dist}}.$$

The order of magnitude of the prefactor $T_{\text{ss}}^{\text{dist}}$ can be obtained using simple dimensional arguments. One finds that

$$T_{\text{ss}}^{\text{dist}} \sim \frac{Q_{\text{ss}}}{k_{\text{peak}}^4} \frac{1}{\tau_{\text{ss}}},$$

where $\tau_{\rm ss}$ is the characteristic time of small scales. Assuming that the order of magnitude of $\mathtt{T}_{\rm ss}^{\mathtt{dist}}$ does not change significantly over a time period of $\tau_{\rm ss}$, distant interactions eventually produce a spectrum $Q_{\rm ss}^{\mathtt{dist}}$ over this period which is on the order of,

$$\text{for } k \ll k_{\rm peak}, \quad Q_{\rm ss}^{\mathtt{dist}} \sim T_{\rm ss}\tau_{\rm ss} \sim Q_{\rm ss}\left(\frac{k}{k_{\rm peak}}\right)^4.$$

Thus, after a time $\tau_{\rm ss}$ and for $k \ll k_{\rm peak}$, $\mathtt{Q}^{\mathtt{so}}$ is the sum of the large-scale initial condition $Q_{\rm ls}(k/k_{\rm peak})^{\sigma_{\rm so}}$ and of the distant interaction spectrum $Q_{\rm ss}^{\mathtt{dist}}$. The two spectral contributions can be compared thanks to a wave number $k_{\rm dist}$ defined by

$$k_{\rm dist} = k_{\rm peak}\left(\frac{Q_{\rm ls}}{Q_{\rm ss}}\right)^{\frac{1}{4-\sigma_{\rm so}}}. \tag{C6}$$

It can be checked that,

$$\text{for } k \gg k_{\rm dist}, \quad Q_{\rm ss}^{\mathtt{dist}} \gg Q_{\rm ls}(k/k_{\rm peak})^{\sigma_{\rm so}} \text{ and, for } k \ll k_{\rm dist}, \quad Q_{\rm ss}^{\mathtt{dist}} \ll Q_{\rm ls}(k/k_{\rm peak})^{\sigma_{\rm so}}.$$

From there, three situations can be distinguished, as illustrated in Fig. 12.

(1) First, for $k_{\rm dist} \ll k_c$, one has $\mathtt{Q}^{\mathtt{so}} \approx Q_{\rm ss}^{\mathtt{dist}} \propto k^4$ over the whole large-scale range [see Fig. 12(a)]. Therefore, during the self-similar evolution of the flow, Θ reaches its minimum value $\Theta_{\rm min} = \frac{1}{4-\eta/2}$ independently of $\sigma_{\rm so}$.

(2) Second, for $k_c \ll k_{\rm dist} \ll k_{\rm peak}$, the large-scale range is divided in two subintervals [see Fig. 12(b)]. For $k_{\rm dist} \ll k \ll k_{\rm peak}$, one has $\mathtt{Q}^{\mathtt{so}} \approx Q_{\rm ss}^{\mathtt{dist}}$ and for $k_c \ll k \ll k_{\rm dist}$, one has $\mathtt{Q}^{\mathtt{so}} \approx Q_{\rm ls}(k/k_{\rm peak})^{\sigma_{\rm so}}$. In that case, Θ displays two successive values. Until the time when $k_{\rm peak}(t) \sim k_{\rm dist}$, Θ is equal to $\Theta_{\rm min}$. After, Θ tends to its $\sigma_{\rm so}$-dependent value given by Eq. (32) and its generalization Eq. (C2). Note that if $\sigma_{\rm so} < 4 - \eta$, an increase in Θ is observed after the transition.

(3) Finally, for $k_{\rm dist} \gg k_{\rm peak}$, one has $\mathtt{Q}^{\mathtt{so}} \approx Q_{\rm ls}(k/k_{\rm peak})^{\sigma_{\rm so}}$ over the whole large-scale range [see Fig. 12(c)]. In that case, the value of Θ is given by Eq. (32) and its generalization Eq. (C2).

Using Eq. (C5), these three situations can be reformulated as a function of the perturbation height variances $\sigma_{\rm ls}^2$ and $\sigma_{\rm ss}^2$. More precisely, when $\sigma_{\rm so} < 0$, and $\alpha \sim 1$, one finds that, for $k \ll k_{\rm peak}$:

$$\mathtt{Q}^{\mathtt{so}} \approx Q_{\rm ss}^{\mathtt{dist}} \quad \text{if} \quad \frac{\sigma_{\rm ls}^2}{\sigma_{\rm ss}^2} \ll \frac{1}{|\sigma_{\rm so}|}\left(\frac{k_c}{k_{\rm peak}}\right)^4 \ll 1 \quad \text{and} \quad \mathtt{Q}^{\mathtt{so}} \approx Q_{\rm ls}(k/k_{\rm peak})^{\sigma_{\rm so}}$$

$$\text{if} \quad \frac{\sigma_{\rm ls}^2}{\sigma_{\rm ss}^2} \gg \frac{1}{|\sigma_{\rm so}|}\left(\frac{k_c}{k_{\rm peak}}\right)^{-|\sigma_{\rm so}|} \gg 1$$

Thus, the conditions for having a pure backscattering spectrum or a preservation of the initial condition are more stringent than simply having $\sigma_{\rm ls}^2 \gg \sigma_{\rm ss}^2$ or $\sigma_{\rm ls}^2 \ll \sigma_{\rm ss}^2$. By contrast, the two subinterval situation is obtained for a large interval of values of the ratio $\sigma_{\rm ls}^2/\sigma_{\rm ss}^2$ and in particular for $\sigma_{\rm ls}^2 \sim \sigma_{\rm ss}^2$.

When $\sigma_{\rm so} > 0$, the previous conclusions are slightly modified. Indeed, one has, for $k \ll k_{\rm peak}$:

$$\mathtt{Q}^{\mathtt{so}} \approx Q_{\rm ss}^{\mathtt{dist}} \quad \text{if} \quad \frac{\sigma_{\rm ls}^2}{\sigma_{\rm ss}^2} \ll \frac{1}{\sigma_{\rm so}}\left(\frac{k_c}{k_{\rm peak}}\right)^{4-\sigma_{\rm so}} \ll 1 \quad \text{and} \quad \mathtt{Q}^{\mathtt{so}} \approx Q_{\rm ls}(k/k_{\rm peak})^{\sigma_{\rm so}} \quad \text{if} \quad \frac{\sigma_{\rm ls}^2}{\sigma_{\rm ss}^2} \gg 1.$$

The conditions for getting a pure backscattering spectrum or a preservation of the initial condition are less demanding than those obtained for $\sigma_{\rm so} < 0$. Accordingly, the two subinterval situation is observed under tighter conditions, and in particular, it does not occur when $\sigma_{\rm ls}^2 \sim \sigma_{\rm ss}^2$.

To conclude on this topic, let us note that when k_c, $k_{\rm dist}$, and $k_{\rm peak}$ are not separated by orders of magnitude, then no clear power-law range can be identified at large scales. Hence, there is no precise value of Θ and probably no well defined self-similar regime. Besides, it is also worth stressing that it is already very computationally demanding to track the self-similar evolution of a flow with a single power-law range at large scales. Being able to follow a flow with two large-scale ranges

would significantly increase the cost of large eddy and direct numerical simulations. This leads us to stress again the speculative nature of the content of this Appendix. The arguments proposed in it are not supported by simulations or experiments and should consequently be considered with care.

APPENDIX D: HAAN'S MODEL

In a recent article [12], Haan's model was used to study the self-similar turbulent regime of mixing zones generated by the Rayleigh–Taylor and Richtmyer–Meshkov instabilities. Haan's model was first proposed in Refs. [38,39] with the purpose of describing the weakly nonlinear regime of these two instabilities. It is designed out of two components. The first one is a second-order expansion allowing us to compute the amplitudes of interfacial modes. It can be applied provided these amplitudes remain small. The second component is a saturation closure which comes into play whenever mode amplitudes become too large and cross a given threshold.

Thus, Haan's expansion and Haan's saturation closure are two distinct elements which are stitched together to yield what is usually referred to as Haan's model [12]. For modes with small amplitudes, Haan's expansion is well-posed and yields unambiguous results. However, difficulties arise whenever the saturation closure becomes active. For weakly nonlinear flows, some of these difficulties have been pointed out by Haan himself [38,39], while others can be found for instance in Refs. [40,41]. In this Appendix, we would like to review these difficulties and also to discuss their impact beyond the weakly nonlinear context, when the flow becomes turbulent and self-similar. The discussion is restricted to the Richtmyer–Meshkov case.

1. Haan's second-order expansion

As explained above, Haan's second-order expansion is one of the two building blocks of Haan's model. For modes with small amplitudes, the derivation of this expansion is unequivocal and is detailed in Ref. [38]. Its expression is recalled in this section when it is applied to the Richtmyer–Meshkov context. To this end, we consider an interface centered around the coordinate $x_3 = 0$ which is deformed by a perturbation of height $h(\boldsymbol{x}_\perp, t)$, where $\boldsymbol{x}_\perp = (x_1, x_2)$ (see Fig. 1). The height function h is decomposed into 2D Fourier modes with a complex amplitude $Z_{\boldsymbol{k}_\perp}$ defined as follows:

$$Z_{\boldsymbol{k}_\perp}(t) = \widehat{h}^{2\mathrm{D}}(\boldsymbol{k}_\perp, t) = \frac{1}{(2\pi)^2} \int e^{-\imath \boldsymbol{k}_\perp \cdot \boldsymbol{x}_\perp} h(\boldsymbol{x}_\perp, t) d\boldsymbol{x}_\perp.$$

By assuming that the component of the velocity normal to the interface is continuous, that the interface moves with the fluid and that the pressure field is constant across the interface (notwithstanding surface tension effects), Haan shows that $Z_{\boldsymbol{k}_\perp}$ obeys the following equation when its modulus $|Z_{\boldsymbol{k}_\perp}|$ is very small:

$$\ddot{Z}_{\boldsymbol{k}_\perp} = \mathtt{A}_t k_\perp g Z_{\boldsymbol{k}_\perp} + \mathtt{A}_t k_\perp \int_{\boldsymbol{a}+\boldsymbol{b}=\boldsymbol{k}_\perp} \left(\dot{Z}_{\boldsymbol{a}}\dot{Z}_{\boldsymbol{b}}\xi_{ab} + \ddot{Z}_{\boldsymbol{a}}Z_{\boldsymbol{b}}\zeta_{ab}\right) d\boldsymbol{a} + \mathcal{O}(Z_{\boldsymbol{k}_\perp}^3),$$

$$\text{with} \quad \xi_{ab} = \frac{1}{2} - \tilde{\boldsymbol{a}} \cdot \tilde{\boldsymbol{k}}_\perp - \frac{1}{2}\tilde{\boldsymbol{a}} \cdot \tilde{\boldsymbol{b}} \quad \text{and} \quad \zeta_{ab} = 1 - \tilde{\boldsymbol{a}} \cdot \tilde{\boldsymbol{k}}_\perp. \tag{D1}$$

In these equations, the notations v and $\tilde{v}$ refer to the norm and direction of a given vector $\boldsymbol{v}$: $v = \sqrt{v_i v_i}$ and $\tilde{\boldsymbol{v}} = \boldsymbol{v}/v$. Besides, time derivatives have been denoted with dots: $\dot{Z}_{\boldsymbol{a}} = \partial_t Z_{\boldsymbol{a}}$ and $\ddot{Z}_{\boldsymbol{a}} = \partial_{tt}^2 Z_{\boldsymbol{a}}$. As for g, it refers to the acceleration applied to the flow and can vary with time. For Richtmyer–Meshkov turbulence, g is chosen impulsive:

$$g(t) = \Delta U \delta(t), \tag{D2}$$

with ΔU a velocity jump mimicking the interface velocity jump due to the shock crossing.

In addition, Eq. (D1) is completed by a set of initial conditions. Just before the impulsive acceleration the interface is assumed to be at rest so that

$$\dot{Z}_{\boldsymbol{k}_\perp}(t = 0^-) = \dot{Z}_{\boldsymbol{k}_\perp}^{0^-} = 0. \tag{D3}$$

However, just after the impulsive acceleration, the interface is put in motion, so that

$$\dot{Z}_{\boldsymbol{k}_\perp}(t = 0^+) = \dot{Z}_{\boldsymbol{k}_\perp}^{0^+} \neq 0.$$

The value of $\dot{Z}_{\boldsymbol{k}_\perp}^{0^+}$ is a result of the integration of Eq. (D1) and will be determined later. As for the amplitude $Z_{\boldsymbol{k}_\perp}$, its evolution is continuous and there is no need to differentiate between its value just before and just after the impulsive acceleration. Its initial condition will simply be denoted by $Z_{\boldsymbol{k}_\perp}^0$:

$$Z_{\boldsymbol{k}_\perp}(t = 0) = Z_{\boldsymbol{k}_\perp}^0.$$

Of particular interest is the case where the initial spectrum of $Z_{\boldsymbol{k}_\perp}$ obeys a power law at small wave numbers as in Eqs. (28) or (B6). To simplify the analysis, this power law will be transcribed directly in terms of the modulus of $Z_{\boldsymbol{k}_\perp}$:

$$\left| Z_{\boldsymbol{k}_\perp}^0 \right| \propto k_\perp^{n_0} \text{ for } k \ll k_{\text{peak}}, \tag{D4}$$

with k_{peak} a given peak wave number. The exponent n_0 is directly related to the infrared exponent m of the power spectrum of the perturbation of Eqs. (28) or (B6) by the relation

$$n_0 = \frac{m - 1}{2}.$$

2. Alternative formulations of Haan's expansion

In Eq. (D1), a $\mathcal{O}(Z_{\boldsymbol{k}_\perp}^3)$ term has been added to recall that the equation derived by Haan is valid up to terms of order $Z_{\boldsymbol{k}_\perp}^3$. With this in mind, we can re-express Eq. (D1) as follows. First, we note that apart from the linear production term, $\ddot{Z}_{\boldsymbol{k}_\perp}$ is of order 2. Therefore, one can replace its occurrence in the convolution product by retaining only this particular contribution. Thus, we can rewrite Eq. (D1) as

$$\ddot{Z}_{\boldsymbol{k}_\perp} = \mathtt{A}_t k_\perp g \left(Z_{\boldsymbol{k}_\perp} + \mathtt{A}_t \int_{\boldsymbol{a}+\boldsymbol{b}=\boldsymbol{k}_\perp} a Z_{\boldsymbol{a}} Z_{\boldsymbol{b}} \zeta_{\boldsymbol{ab}} \, d\boldsymbol{a} \right) + \mathtt{A}_t k_\perp \int_{\boldsymbol{a}+\boldsymbol{b}=\boldsymbol{k}_\perp} \dot{Z}_{\boldsymbol{a}} \dot{Z}_{\boldsymbol{b}} \xi_{\boldsymbol{ab}} \, d\boldsymbol{a} + \mathcal{O}(Z_{\boldsymbol{k}_\perp}^3). \tag{D5}$$

This formulation is interesting as it shows explicitly that even if $Z_{\boldsymbol{k}_\perp} = 0$ at a given time and a given $\boldsymbol{k}_\perp$, nonlinear interactions will still trigger some form of buoyancy production thanks to the term involving $\zeta_{\boldsymbol{ab}}$. Another interest of this formulation is that it can be compared more easily with the ones used in other references. For instance, in Ref. [12], the following simplification of Haan's second-order expansion is proposed in the Richtmyer–Meshkov case:

$$\text{Haan's expansion in Ref. [12]}: \quad \ddot{Z}_{\boldsymbol{k}_\perp} = \mathtt{A}_t k_\perp g Z_{\boldsymbol{k}_\perp} + \mathtt{A}_t k_\perp \int_{\boldsymbol{a}+\boldsymbol{b}=\boldsymbol{k}_\perp} \dot{Z}_{\boldsymbol{a}} \dot{Z}_{\boldsymbol{b}} \xi_{\boldsymbol{ab}} \, d\boldsymbol{a}, \tag{D6}$$

where the value of $\dot{Z}_{\boldsymbol{k}_\perp}$ in the convolution product is directly replaced by its linear approximation just after the impulsive acceleration, i.e., by $\mathtt{A}_t k_\perp \Delta U Z_{\boldsymbol{k}_\perp}^0$. Comparing Eqs. (D5) and (D6), one can see that the nonlinear term involving $\zeta_{\boldsymbol{ab}}$ has been discarded in Ref. [12]. An immediate consequence is the following. Integrating Eqs. (D5) and (D6) from $t = 0^-$ to $t = 0^+$, one finds

$$\text{Eq. (D6) from this work}: \quad \dot{Z}_{\boldsymbol{k}_\perp}^{0^+} = \mathtt{A}_t k_\perp \Delta U \left(Z_{\boldsymbol{k}_\perp}^0 + \mathtt{A}_t \int_{\boldsymbol{a}+\boldsymbol{b}=\boldsymbol{k}_\perp} a Z_{\boldsymbol{a}}^0 Z_{\boldsymbol{b}}^0 \zeta_{\boldsymbol{ab}} \, d\boldsymbol{a} \right), \tag{D7}$$

$$\text{Eq. (D6) from Ref. [12]}: \quad \dot{Z}_{\boldsymbol{k}_\perp}^{0^+} = \mathtt{A}_t k_\perp \Delta U Z_{\boldsymbol{k}_\perp}^0. \tag{D8}$$

Thus, the nonlinear component of the initial impulse given to the interface is missing in Ref. [12]. This difference is especially striking when considering an initial annular spectrum (i.e., such that $Z_{\boldsymbol{k}_\perp}^0 = 0$ except in when $k_\perp$ is in a given finite interval centered around k_{peak}). Then, for $k_\perp \ll k_{\text{peak}}$, $\dot{Z}_{\boldsymbol{k}_\perp}^{0^+} = 0$ according to Ref. [12] even though it is not according to the full version of the nonlinear expansion. A similar comment applies to other references, such as Refs. [39,42].

The reformulation of Eq. (D1) can be led further and, to some extent, made arbitrary. Starting from the relation $\dot{Z}_a\dot{Z}_b = \partial_{tt}^2(Z_aZ_b)/2 - (\ddot{Z}_aZ_b + \ddot{Z}_bZ_a)/2$, we can add the left-hand side of this equality and subtract its right-hand side to the integrand appearing in Eq. (D1). Furthermore, the added and subtracted terms can be weighted by an arbitrary function of a and b that will be denoted by η_{ab}. Finally, after performing these operations, we can convert the second-order derivatives as we did previously, by neglecting terms of order $Z_{\boldsymbol{k}_\perp}^3$ or higher. As a result, we obtain that Haan's expansion can be written as

$$\ddot{Z}_{\boldsymbol{k}_\perp} = \mathtt{A}_t k_\perp g\left(Z_{\boldsymbol{k}_\perp} + \frac{1}{2}\mathtt{A}_t \mathcal{G}_{\boldsymbol{k}_\perp}\right) + \frac{1}{2}\mathtt{A}_t k_\perp \partial_{tt}^2 \mathcal{H}_{\boldsymbol{k}_\perp} + \mathtt{A}_t k_\perp \mathcal{I}_{\boldsymbol{k}_\perp} + \mathcal{O}(Z_{\boldsymbol{k}_\perp}^3), \tag{D9}$$

$$\text{with} \quad \mathcal{G}_{\boldsymbol{k}_\perp} = \int_{\boldsymbol{a}+\boldsymbol{b}=\boldsymbol{k}_\perp} Z_a Z_b \left(a\zeta_{ab} - \eta_{ab}\frac{a+b}{2}\right) d\boldsymbol{a}, \tag{D10}$$

$$\mathcal{H}_{\boldsymbol{k}_\perp} = \int_{\boldsymbol{a}+\boldsymbol{b}=\boldsymbol{k}_\perp} Z_a Z_b \eta_{ab}\, d\boldsymbol{a}, \tag{D11}$$

$$\mathcal{I}_{\boldsymbol{k}_\perp} = \int_{\boldsymbol{a}+\boldsymbol{b}=\boldsymbol{k}_\perp} \dot{Z}_a \dot{Z}_b (\xi_{ab} - \eta_{ab})\, d\boldsymbol{a}. \tag{D12}$$

Thus, one can arbitrarily split the nonlinear term of Haan's expansion into three distinct contributions: the first one, $\mathcal{G}_{\boldsymbol{k}_\perp}$, ties buoyancy production and nonlinearities, the second one, $\mathcal{H}_{\boldsymbol{k}_\perp}$, is written in a conservative form and involves the second-order time derivative of a convolution product of $Z_{\boldsymbol{k}_\perp}$ with itself, and the last one, $\mathcal{I}_{\boldsymbol{k}_\perp}$, is a source term involving the convolution product of $\dot{Z}_{\boldsymbol{k}_\perp}$ with itself. With $\eta_{ab} = 0$, one suppresses the conservative contribution and finds Eq. (D1). Besides, with $\eta_{ab} = \xi_{ab}$, the source term $\mathcal{I}_{\boldsymbol{k}_\perp}$ is suppressed while, with $\eta_{ab} = \frac{2a}{a+b}\zeta_{ab}$, it is $\mathcal{G}_{\boldsymbol{k}_\perp}$ which is null.

As long as $|Z_{\boldsymbol{k}_\perp}|$ is small, the particular choice of η_{ab} is not important: whatever its value, Eq. (D9) yields an equivalent description of the evolution of $Z_{\boldsymbol{k}_\perp}$ up to terms of order $\mathcal{O}(Z_{\boldsymbol{k}_\perp}^3)$. However, when $|Z_{\boldsymbol{k}_\perp}|$ is not small, the different contributions appearing in its right-hand side cannot be interchanged any longer. In that case, the particular choice of η_{ab} has consequences on the properties of Haan's expansion and on its role in the evaluation Θ.

3. Value of Θ in Haan's model

Haan's expansion is often used beyond its domain of validity to describe the evolution of weakly nonlinear flows and even turbulent mixing zones [12]. In that case, Haan's expansion is stitched with a saturation closure, examples of which can be found in Refs. [12,39]. More precisely, with the saturation closure detailed in Ref. [12], three types of modes can be distinguished. First, Haan's expansion is used to describe the evolution of small amplitude modes. It is applied when $Z_{\boldsymbol{k}_\perp}$ is below a threshold, called saturation amplitude and noted $Z_{\boldsymbol{k}_\perp}^{\text{sat}}$. The latter is generally modeled as follows:

$$Z_{\boldsymbol{k}_\perp}^{\text{sat}} = s_1 k_\perp^{-2}, \tag{D13}$$

with s_1 a model constant. Second, modes with an amplitude larger than $Z_{\boldsymbol{k}_\perp}^{\text{sat}}$ and smaller than a second threshold noted $Z_{\boldsymbol{k}_\perp}^{\text{froz}}$ undergo an evolution which is not driven by Haan's expansion but is instead closed using dimensional arguments. These modes are called saturated modes and their upper threshold $Z_{\boldsymbol{k}_\perp}^{\text{froz}}$ is equal to a few times $Z_{\boldsymbol{k}_\perp}^{\text{sat}}$:

$$Z_{\boldsymbol{k}_\perp}^{\text{froz}} = s_2 k_\perp^{-2}, \quad \text{with} \quad s_2 > s_1. \tag{D14}$$

Finally, modes with an amplitude larger than this second threshold are frozen: their amplitude does not evolve in time any longer. This decomposition has been formulated in terms of the amplitudes $Z_{\boldsymbol{k}_\perp}$ of the modes. It can also be expressed by introducing three distinct spectral ranges: a nonsaturated small wave number range for $k_\perp \leqslant k_s(t)$, a saturated intermediate wave number range for $k_s(t) \leqslant k_\perp \leqslant k_f(t)$, and an frozen high-wave-number range for $k_\perp \geqslant k_f(t)$.

At first sight, it would appear that restricting Haan's expansion to small-amplitude modes guarantees that it is correctly used. However, this is deceptive: the convolution products in Haan's expansion involve modes pertaining to the saturated and frozen ranges, with amplitudes that are consequently not small. In Ref. [12], this issue is partially addressed by eliminating the frozen range from convolution products. However, saturated modes remain. Thus, even though it is not applied to the saturated and frozen ranges, Haan's expansion is still applied beyond its domain of validity when used to describe turbulent flows.

To illustrate the ambiguities that ensue, let us introduce the axisymmetric spectrum of $Z_{k_\perp}$ and its integral $\overline{Z^2}$:

$$\overline{Z^2} = 2\pi \int k_\perp E_Z(k_\perp) dk_\perp \quad \text{with} \quad E_Z(k_\perp)\delta(\boldsymbol{k}_\perp + \boldsymbol{k}'_\perp) = \overline{Z_{\boldsymbol{k}_\perp} Z_{\boldsymbol{k}'_\perp}}.$$

The variance $\overline{Z^2}$ is used as the main (often the sole) diagnostic of Haan's turbulence model. Indeed, when the mixing zone is turbulent, the interface separating the fluids is multivalued so that $Z_{\boldsymbol{k}_\perp}$ cannot be associated any longer with the Fourier transform of the height of a single-valued perturbation. Nonetheless, the integral of the spectrum of $Z_{\boldsymbol{k}_\perp}$ still gives access to a characteristic length. The latter is then generally said to correspond to the size of the mixing zone L:

$$L \propto \sqrt{\overline{Z^2}}.$$

Thus, when Haan's model is used in the turbulent regime, $Z_{\boldsymbol{k}_\perp}$ has become a proxy for computing L and does not appear to bear any physical meaning beyond this purpose.

The contribution to $\overline{Z^2}$ from wave numbers smaller than K is denoted by $\overline{Z^2}_K$ and defined by

$$\overline{Z^2}_K = 2\pi \int_0^K k_\perp E_Z(k_\perp) dk_\perp.$$

In the self-similar regime, we assume that $\overline{Z^2}$ and its large-scale contribution share the same time evolution. In other words, we assume that,

$$\text{for} \quad \frac{K}{k_s} = \epsilon \ll 1, \quad \overline{Z^2}_K \propto \overline{Z^2} \propto t^{2\Theta}.$$

With this hypothesis, we can analyze the self-similar properties of the flow by looking at the properties of the spectrum E_Z at small wave numbers. Integrating Eq. (D9) and dropping third-order terms, we deduce that

$$\text{for} \quad \frac{k_\perp}{k_s} \ll 1, Z_{\boldsymbol{k}_\perp} = Z_{\boldsymbol{k}_\perp}^0 + \mathtt{A}_t \Delta U k_\perp t \left(Z_{\boldsymbol{k}_\perp}^0 + \frac{1}{2}\mathtt{A}_t \mathcal{G}_{\boldsymbol{k}_\perp}^0\right) + \frac{1}{2}\mathtt{A}_t k_\perp\left(\mathcal{H}_{\boldsymbol{k}_\perp} - \mathcal{H}_{\boldsymbol{k}_\perp}^0\right)$$

$$+ \mathtt{A}_t k_\perp \int_0^t \int_0^{t'} \mathcal{I}_{\boldsymbol{k}_\perp}(t'') dt'' dt'. \tag{D15}$$

As a result, the spectrum of $Z_{\boldsymbol{k}_\perp}$ takes the following form at small wave numbers,

$$\text{for} \quad \frac{k_\perp}{k_s} \ll 1, \quad E_Z(k_\perp) = E_Z^0(k_\perp)(1 + \mathtt{A}_t \Delta U k_\perp t)^2 + \frac{1}{4}\mathtt{A}_t^4 \Delta U^2 E_{GG}^0(k_\perp) k_\perp^2 t^2 + \frac{1}{4}\mathtt{A}_t^2 E_{HH}(k_\perp, t) k_\perp^2$$

$$+ \mathtt{A}_t^2 E_{II}(k_\perp, t) k_\perp^2 + \text{cross terms}, \tag{D16}$$

where E_Z^0 is the initial value of E_Z and where E_{GG}^0, E_{HH}, and E_{II} are, respectively, the spectra of $\mathcal{G}_{\boldsymbol{k}_\perp}^0$, $\mathcal{H}_{\boldsymbol{k}_\perp} - \mathcal{H}_{\boldsymbol{k}_\perp}^0$, and $\int_0^t \int_0^{t'} \mathcal{I}_{\boldsymbol{k}_\perp}(t'') dt'' dt'$. In the definitions of $\mathcal{G}_{\boldsymbol{k}_\perp}$, $\mathcal{H}_{\boldsymbol{k}_\perp}$, and $\mathcal{I}_{\boldsymbol{k}_\perp}$, we introduced an arbitrary parameter η_{ab}. Here, we would like to specify it as follows:

$$\eta_{ab} = \frac{2a}{a+b}\left[\zeta_{ab} - \eta_0\left(\frac{k_\perp}{a}\right)^{\sigma_\eta}\right].$$

With this particular definition, a distant interaction approximation of the spectra E_{GG}^0, E_{HH}, and E_{II} yields,

$$\text{for } \frac{k_\perp}{k_s} \ll 1, \quad E_{GG}^0 = C_G k_\perp^{2\sigma_\eta}, \quad E_{HH} = C_H(t) k_\perp^0, \quad \text{and} \quad E_{II} = C_I(t) k_\perp^{2\min(\sigma_\eta, 1)},$$

where the coefficients $C_H(t)$ and $C_I(t)$ depend on the most energetic scales of the spectrum and undergo a self-similar evolution. Using these expressions, integrating the spectrum up to $K(t) = \epsilon k_s(t)$ and assuming that t is large, we find that,

$$\text{for } \frac{K}{k_s} = \epsilon \ll 1, \quad \frac{\overline{Z^2}_K}{2\pi} = \mathbb{A}_t^2 \Delta U^2 \frac{C}{m+3} K(t)^{m+3} t^2 + \frac{1}{4} \mathbb{A}_t^4 \Delta U^2 \frac{C_G}{4 + 2\sigma_\eta} K(t)^{4+2\sigma_\eta} t^2$$

$$+ \frac{1}{4} \mathbb{A}_t^2 C_H(t) K(t)^4 + \mathbb{A}_t^2 \frac{C_I(t)}{4 + 2\min(\sigma_\eta, 1)} K(t)^{4 + 2\min(\sigma_\eta, 1)} + \text{cross terms}. \tag{D17}$$

In the self-similar regime, the left-hand side is proportional to $t^{2\Theta}$. Besides, the coefficients $C_H(t)$ and $C_I(t)$ evolve self-similarly and so does $K(t)$. Then, dimensional analysis implies that the last two terms of the right-hand side are also proportional to $t^{2\Theta}$. As for the first two terms on the right-hand side, they are, respectively, proportional to $t^{2-(m+3)\Theta}$ and to $t^{2-(4+2\sigma_\eta)\Theta}$. Therefore, we find that

$$\Theta = \frac{2}{\min(m, m_{\text{haan}}) + 5}, \quad \text{with} \quad m_{\text{haan}} = 1 + 2\sigma_\eta.$$

Thus, the minimum value of Θ in Haan's model depends on the arbitrary expression given to its associated second-order expansion. In our case, the value of $\Theta_{\min}$ depends on the arbitrary parameter σ_η:

$$\Theta_{\min} = \frac{1}{3 + \sigma_\eta}.$$

For $\sigma_\eta = -3/2$, we obtain $\Theta_{\min} = 2/3$, for $\sigma_\eta = 0$, we obtain $\Theta_{\min} = 1/3$, for $\sigma_\eta = 1$, we obtain $\Theta_{\min} = 1/4$, and for $\sigma_\eta = 2$, we obtain $\Theta_{\min} = 1/5$.

The main conclusion is that, by itself, Haan's model is not sufficient to predict the limit value of Θ. The fundamental reason is that Haan's expansion is ill posed whenever modes with large amplitudes are involved. This is necessarily the case when distant interactions dominate nonlinear interactions. Unfortunately, these distant interactions are precisely the ones which determine the value of $\Theta_{\min}$.

Note that the arbitrary decomposition that we introduced in Eq. (D9) is only one among many others. For instance, in Eq. (D5) one could also have made the substitution $\dot{Z}_{k_\perp} = \alpha \dot{Z}_{k_\perp} + (1 - \alpha)\mathbb{A}_t \Delta U k_\perp Z_{k_\perp}^0$ with α another arbitrary parameter. This substitution is valid up to $\mathcal{O}(Z_{k_\perp}^3)$ in Haan's expansion and would lead to different values of $\Theta_{\min}$. Note also that several authors [12] choose to prevent modes from contributing to nonlinear convolution products and to distant interactions, shortly after they have saturated. Again, there are several ways of enforcing this condition, each leading to different values of Θ.

4. Solenoidal momentum

In this subsection and the next one, we leave aside Haan's turbulent model and the value of Θ. We turn our focus back on the properties of Haan's expansion within its rightful domain of validity. Our aim is to derive the evolution equation of the solenoidal momentum s associated with Haan's expansion. To this end, we use the fact that Haan's expansion is derived by assuming that the velocity u is potential below and above the interface $x_3 = h(x_\perp)$. Following Haan, we denote by ϕ_H and ϕ_L the velocity potentials in the upper and lower fluids, and by ρ_H and ρ_L the corresponding densities. Then, with H the Heaviside function, we can write that the momentum is given by

$$\rho u = -\rho_H \nabla \phi_H H[x_3 - h(x_\perp)] - \rho_L \nabla \phi_L H[h(x_\perp) - x_3]. \tag{D18}$$

The 2D Fourier transforms of these potentials are defined by

$$\widehat{\phi}_H^{2D}(\boldsymbol{k}_\perp, x_3) = \frac{1}{(2\pi)^2} \int e^{-\imath \boldsymbol{k}_\perp \cdot \boldsymbol{x}_\perp} \phi_H(\boldsymbol{x}) d\boldsymbol{x}_\perp \quad \text{and} \quad \widehat{\phi}_L^{2D}(\boldsymbol{k}_\perp, x_3) = \frac{1}{(2\pi)^2} \int e^{-\imath \boldsymbol{k}_\perp \cdot \boldsymbol{x}_\perp} \phi_H(\boldsymbol{x}) d\boldsymbol{x}_\perp.$$

To satisfy the incompressible relations $\nabla^2 \phi_H = \nabla^2 \phi_L = 0$, Haan proposes the following x_3-dependency for these transforms:

$$\widehat{\phi}_H^{2D}(\boldsymbol{k}_\perp, x_3) = \varphi_H(\boldsymbol{k}_\perp) e^{-k_\perp x_3} \quad \text{and} \quad \widehat{\phi}_L^{2D}(\boldsymbol{k}_\perp, x_3) = \varphi_L(\boldsymbol{k}_\perp) e^{k_\perp x_3}. \tag{D19}$$

The fact that the interface moves with the fluid and that the normal velocity is continuous implies that the two functions φ_H and φ_L are related to the perturbation amplitude $Z_{\boldsymbol{k}_\perp}$ as follows:

$$\varphi_H(\boldsymbol{k}_\perp) = \frac{\dot{Z}_{\boldsymbol{k}_\perp}}{k_\perp} + \langle \varphi \rangle + \mathcal{O}(Z_{\boldsymbol{k}_\perp}^3) \quad \text{and} \quad \varphi_L(\boldsymbol{k}_\perp) = -\frac{\dot{Z}_{\boldsymbol{k}_\perp}}{k_\perp} + \langle \varphi \rangle + \mathcal{O}(Z_{\boldsymbol{k}_\perp}^3), \tag{D20}$$

$$\text{with} \quad \langle \varphi \rangle = \frac{\varphi_H + \varphi_L}{2} = \tilde{\boldsymbol{k}}_\perp \cdot \int_{\boldsymbol{a}+\boldsymbol{b}=\boldsymbol{k}_\perp} \tilde{\boldsymbol{b}} \, \dot{Z}_{\boldsymbol{b}} Z_{\boldsymbol{a}} \, d\boldsymbol{a}. \tag{D21}$$

The properties of the velocity potentials being specified, we can now turn our attention to the evaluation of the solenoidal component of the momentum $\boldsymbol{s}$. The fluctuating part of $\boldsymbol{s}$ is defined in spectral space by Eq. (A4) and its full version is given by a similar equation:

$$\widehat{s}_i(\boldsymbol{k}, t) = P_{ij}(\tilde{\boldsymbol{k}}) \widehat{\rho u_j}(\boldsymbol{k}, t),$$

where we used 3D Fourier transforms and where P_{ij} is defined by Eq. (24).

Introducing the alternative notation TF^{2D} and TF^{3D} for the 2D and 3D Fourier transforms, we can combine Eq. (D18) with the definition of $\widehat{\boldsymbol{s}}$ to obtain

$$\widehat{s}_i = P_{ij} \text{TF}^{3D}(-\partial_j \{\rho_H \phi_H \text{H}[x_3 - h(\boldsymbol{x}_\perp)] + \rho_L \phi_L \text{H}[h(\boldsymbol{x}_\perp) - x_3]\}$$
$$+ (\rho_H \phi_H - \rho_L \phi_L)(\delta_{j3} - \partial_j h)\delta[x_3 - h(\boldsymbol{x}_\perp)]).$$

The first group of terms on the right-hand side being a gradient, its Fourier transform is proportional to $\imath k_j$. As a result, it vanishes when multiplied by P_{ij}. Thus, the term proportional to the Dirac function is the only one contributing to $\widehat{s}_i$. Separating the integration over x_3 and $\boldsymbol{x}_\perp$, we can then write that

$$\widehat{s}_i = P_{ij} \text{TF}^{2D} \left\{ \frac{1}{2\pi} \int e^{-\imath k_3 x_3} (\rho_H \phi_H - \rho_L \phi_L)(\delta_{j3} - \partial_j h)\delta[x_3 - h(\boldsymbol{x}_\perp)] dx_3 \right\}$$
$$= \frac{P_{ij}}{2\pi} \text{TF}^{2D}[e^{-\imath k_3 h}(\rho_H \phi_H - \rho_L \phi_L)|_{x_3=h}(\delta_{j3} - \partial_j h)].$$

Following the procedure proposed by Haan, we Taylor expand this expression and retain terms of order 2 in h and ϕ. This yields

$$\widehat{s}_i = \frac{P_{ij}}{2\pi} \text{TF}^{2D}[(\delta_{j3} - \partial_j h - \imath k_3 h \delta_{j3})(\rho_H \phi_H - \rho_L \phi_L)|_{x_3=0} + \delta_{j3} h \partial_3(\rho_H \phi_H - \rho_L \phi_L)|_{x_3=0}] + \text{H.O.T.}, \tag{D22}$$

with H.O.T. referring to higher-order terms. Besides, according to Eq. (D19), we have

$$\text{TF}^{2D}[(\rho_H \phi_H - \rho_L \phi_L)|_{x_3=0}] = \rho_H \varphi_H - \rho_L \varphi_L \quad \text{and} \quad \text{TF}^{2D}[\partial_3(\rho_H \phi_H - \rho_L \phi_L)|_{x_3=0}]$$
$$= -k_\perp(\rho_H \varphi_H + \rho_L \varphi_L).$$

Then, according to Eq. (D20), we deduce that

$$\text{TF}^{2D}[(\rho_H \phi_H - \rho_L \phi_L)|_{x_3=0}] = 2\langle \rho \rangle \left(\frac{\dot{Z}_{\boldsymbol{k}_\perp}}{k_\perp} + \text{A}_t \langle \varphi \rangle \right) + \mathcal{O}(Z_{\boldsymbol{k}_\perp}^3) \tag{D23}$$

and $\quad \text{TF}^{\text{2D}}[\partial_3(\rho_H\phi_H - \rho_L\phi_L)|_{x_3=0}] = -2\langle\rho\rangle k_\perp\left(\text{A}_t\frac{\dot{Z}_{\boldsymbol{k}_\perp}}{k_\perp} + \langle\varphi\rangle\right) + \mathcal{O}\big(Z_{\boldsymbol{k}_\perp}^3\big),$ (D24)

with $\langle\rho\rangle = (\rho_H + \rho_L)/2$. Injecting these expressions into the convolution products appearing in Eq. (D22), we obtain that

$$\frac{\pi}{\langle\rho\rangle}\widehat{s_i} = P_{i3}\left(\frac{\dot{Z}_{\boldsymbol{k}_\perp}}{k_\perp} - \text{A}_t\int_{\boldsymbol{a}+\boldsymbol{b}=\boldsymbol{k}_\perp}\dot{Z}_{\boldsymbol{a}}Z_{\boldsymbol{b}}\zeta_{ab}\,d\boldsymbol{a}\right) + \iota P_{ij}\int_{\boldsymbol{a}+\boldsymbol{b}=\boldsymbol{k}_\perp}\tilde{a}_j\dot{Z}_{\boldsymbol{a}}Z_{\boldsymbol{b}}\,d\boldsymbol{a} + \mathcal{O}\big(Z_{\boldsymbol{k}_\perp}^3\big). \quad (D25)$$

Taking the time derivative of this expression and replacing the value of $\ddot{Z}_{\boldsymbol{k}_\perp}$ by Eq. (D5), we derive the following evolution equation for s:

$$\frac{\pi}{\langle\rho\rangle}\partial_t\widehat{s_i} = \text{A}_t g P_{i3}\left(Z_{\boldsymbol{k}_\perp} - \frac{\iota}{2}k_3\int_{\boldsymbol{a}+\boldsymbol{b}=\boldsymbol{k}_\perp}Z_{\boldsymbol{a}}Z_{\boldsymbol{b}}\,d\boldsymbol{a}\right) - \frac{1}{2}\text{A}_t P_{i3}\int_{\boldsymbol{a}+\boldsymbol{b}=\boldsymbol{k}_\perp}\dot{Z}_{\boldsymbol{a}}\dot{Z}_{\boldsymbol{b}}(1 + \tilde{\boldsymbol{a}}\cdot\tilde{\boldsymbol{b}})\,d\boldsymbol{a} + \iota P_{ij}\int_{\boldsymbol{a}+\boldsymbol{b}=\boldsymbol{k}_\perp}\tilde{a}_j\dot{Z}_{\boldsymbol{a}}\dot{Z}_{\boldsymbol{b}}\,d\boldsymbol{a}$$
$$+ \mathcal{O}\big(Z_{\boldsymbol{k}_\perp}^3\big). \quad (D26)$$

This equation is valid whether the acceleration g is impulsive or not. When g is impulsive, the evolution of s can be expressed by separating its post-shock initial condition and evolution:

$$\text{For } t = 0^+, \quad \frac{\pi}{\langle\rho\rangle}\widehat{s_i} = \text{A}_t\Delta U P_{i3}\left(Z_{\boldsymbol{k}_\perp}^0 - \frac{\iota}{2}k_3\int_{\boldsymbol{a}+\boldsymbol{b}=\boldsymbol{k}_\perp}Z_{\boldsymbol{a}}^0 Z_{\boldsymbol{b}}^0\,d\boldsymbol{a}\right) + \mathcal{O}\big(Z_{\boldsymbol{k}_\perp}^3\big), \quad (D27)$$

$$\text{for } t \geqslant 0^+, \quad \frac{\pi}{\langle\rho\rangle}\partial_t\widehat{s_i} = -\frac{1}{2}\text{A}_t P_{i3}\int_{\boldsymbol{a}+\boldsymbol{b}=\boldsymbol{k}_\perp}\dot{Z}_{\boldsymbol{a}}\dot{Z}_{\boldsymbol{b}}(1 + \tilde{\boldsymbol{a}}\cdot\tilde{\boldsymbol{b}})\,d\boldsymbol{a} + \iota P_{ij}\int_{\boldsymbol{a}+\boldsymbol{b}=\boldsymbol{k}_\perp}\tilde{a}_j\dot{Z}_{\boldsymbol{a}}\dot{Z}_{\boldsymbol{b}}\,d\boldsymbol{a} + \mathcal{O}\big(Z_{\boldsymbol{k}_\perp}^3\big). \quad (D28)$$

As previously mentioned, a term is missing in the expansion used in Ref. [12]. This missing term leaves the post-shock evolution of s unchanged. However, it affects the value of the post-shock initial condition. Instead of the correct expression, Eq. (D27), the following erroneous one is obtained:

$$\text{For } t = 0^+, \quad \frac{\pi}{\langle\rho\rangle}\widehat{s_i} = \text{A}_t\Delta U P_{i3}\left(Z_{\boldsymbol{k}_\perp}^0 - \frac{\iota}{2}k_3\int_{\boldsymbol{a}+\boldsymbol{b}=\boldsymbol{k}_\perp}Z_{\boldsymbol{a}}^0 Z_{\boldsymbol{b}}^0\,d\boldsymbol{a} - \text{A}_t\int_{\boldsymbol{a}+\boldsymbol{b}=\boldsymbol{k}_\perp}a Z_{\boldsymbol{a}}^0 Z_{\boldsymbol{b}}^0\zeta_{ab}\,d\boldsymbol{a}\right). \quad (D29)$$

A cancellation does not take place and an additional term wrongly appears. As will be seen below, this additional term modifies the small wave number asymptotic of $s(t = 0^+)$.

5. Permanence of large-eddies for Haan's expansion

We now consider a spectrum peaked at $k_\perp = k_{\text{peak}}$, as in Eq. (D4), and we expand the different relations we obtained for $k \ll k_{\text{peak}}$ using a distant interaction hypothesis. The following large-scale evolution of s is then derived from Eq. (D28), by assuming that the modulus of $Z_{\boldsymbol{k}_\perp}$ is isotropic and that $Z_{\boldsymbol{k}_\perp}$ is differentiable:

$$\text{For } t \geqslant 0^+ \quad \text{and} \quad k \ll k_{\text{peak}}, \quad \frac{\pi}{\langle\rho\rangle}\partial_t\widehat{s_i} = k^2\mathcal{S}_i(\tilde{\boldsymbol{k}}, t) + \mathcal{O}\big(Z_{\boldsymbol{k}_\perp}^3\big), \quad (D30)$$

$$\text{with} \quad \mathcal{S}_i(\tilde{\boldsymbol{k}}, t) = -\frac{\pi}{4}\text{A}_t P_{i3}\frac{k_\perp^2}{k^2}\int_{a\sim k_{\text{peak}}}\frac{|\dot{Z}_{\boldsymbol{a}}|^2}{a}\,d\boldsymbol{a} + \iota P_{ij}\frac{k_{\perp,k}k_{\perp,l}}{k^2}\int_{a\sim k_{\text{peak}}}\frac{\tilde{a}_j\tilde{a}_k}{a}\dot{Z}_{\boldsymbol{a}}\partial_{a_l}\dot{Z}_{\boldsymbol{a}}^*\,d\boldsymbol{a}. \quad (D31)$$

Then, if we considered that this expression did not come from a Taylor expansion, the evolution of the spectrum Q^{so} of s would take the following form:

$$\partial_t\text{Q}^{\text{so}} = k^6\,\text{T}^{\text{haan}}(t), \quad (D32)$$

with $\text{T}^{\text{haan}}(t)\delta(\boldsymbol{k}_\perp - \boldsymbol{k}'_\perp) = \int_0^t\oint\overline{\mathcal{S}_i(\tilde{\boldsymbol{k}}, t)\mathcal{S}_i^*(\tilde{\boldsymbol{k}}', t')}dS_k dt'$. Therefore, we would predict a backscattering term with an infrared exponent of 6, larger than the value of 4 derived in Eq. (15). As a consequence, large eddies would be permanent up to an infrared exponent of 6 instead of 4.

However, the right-hand side of Eq. (D30) corresponds to the second-order term of a Taylor expansion and yields a fourth order term in the evolution Eq. (D32) of $\mathbb{Q}^{so}$. The issue here is that other fourth order terms are not accounted for in this equation: those involving the product of the first and third orders of $Z_{k_\perp}$. Therefore, the comparison between Eqs. (15) and (D32) suggests that the discarded third order quantities of Haan's expansion are responsible for the main scaling of the nonlinear backscattering term driving the evolution of $\mathbb{Q}^{so}$, while second-order quantities only yield a subdominant backscattering contribution. It is worth stressing that the missing contribution of third-order terms has already been pointed out in Refs. [40,41], where a full description of these terms is proposed.

In any case, the nonlinear terms retained in Haan's truncated expansion do not appear to create a k^2 scaling for $\mathbb{Q}^{so}$. The conditions required to obtain a minimum value of Θ equal to $1/3$ are consequently not provided by Haan's truncated expansion. This aspect is mentioned because a $1/3$ minimum value has been predicted using Haan's saturation closure in Ref. [12]. As we saw in the previous subsections, this prediction is actually not a result of Haan's expansion. Instead, it is linked to the way this expansion is bridged with saturated and frozen modes.

As a final note, the initial spectrum associated with Eq. (D27) for an initial spectrum obeying a power law at small wave numbers [Eq. (D4)] is almost the same as the one already given in Appendix B. Differences arising again from the neglect of third order quantities are nonetheless present. Still, at small wave numbers, the initial condition Eq. (D27) agrees with Eq. (29). By contrast, because of the term neglected in Ref. [12], the initial condition associated with Eq. (D29) would take the form, for $k \ll k_{\text{peak}}$, $\mathbb{Q}^{so}(k, t = 0^+) = C_{so}k^{\sigma_{so}} + \mathcal{O}(k^2)$, where σ_{so} and C_{so} are defined as in Eq. (30). As a result, with the model used in Ref. [12], initial spectra with an infrared exponent larger than 2 would not be allowed, leading to the wrong prediction $\Theta_{\text{min}} = 1/3$. This is of course not the case, as explained in Appendix B.

---

[1] R. D. Richtmyer, Taylor instability in shock acceleration of compressible fluids, Commun. Pure Appl. Math. **13**, 297 (1960).

[2] E. E. Meshkov, Instability of the interface of two gases accelerated by a shock wave, Fluid Dyn. **4**, 101 (1969).

[3] M. Brouillette and B. Sturtevant, Experiments on the Richtmyer-Meshkov instability: Single-scale perturbations on a continuous interface, J. Fluid Mech. **263**, 271 (1994).

[4] Y. Zhou, Rayleigh–Taylor and Richtmyer–Meshkov instability induced flow, turbulence, and mixing I, Phys. Rep. **720-722**, 1 (2017).

[5] Y. Zhou, Rayleigh–Taylor and Richtmyer–Meshkov instability induced flow, turbulence, and mixing II, Phys. Rep. **723-725**, 1 (2017).

[6] Y. Zhou, R. J. R. Williams, P. Ramaprabhu, M. Groom, B. Thornber, A. Hillier, W. Mostert, B. Rollin, S. Balachandar, P. D. Powell, A. Mahalov, and N. Attal, Rayleigh–Taylor and Richtmyer–Meshkov instabilities: A journey through scales, Physica D: Nonlinear Phenomena **423**, 132838 (2021).

[7] G. Birkhoff, Taylor instability and laminar mixing, Technical report (Los Alamos Scientific Lab., NM, 1954), https://doi.org/10.2172/4372366.

[8] N. A. Inogamov, The role of Rayleigh–Taylor and Richtmyer–Meshkov instabilities in astrophysics: An introduction, Astrophys. Space Phys. **10**, 1 (1999).

[9] D. L. Youngs, Effect of initial conditions on self-similar turbulent mixing, In *Proceedings of the 9th International Workshop on the Physics of Compressible Turbulent Mixing (IWPCTM'04)*, Cambridge, UK (2004), available online at http://www.iwpctm.org.

[10] B. Thornber, D. Drikakis, D. L. Youngs, and R. J. R. Williams, The influence of initial conditions on turbulent mixing due to Richtmyer–Meshkov instability, J. Fluid Mech. **654**, 99 (2010).

[11] U. Alon, J. Hecht, D. Mukamel, and D. Shvarts, Scale Invariant Mixing Rates of Hydrodynamically Unstable Interfaces, Phys. Rev. Lett. **72**, 2867 (1994).

[12] Y. Elbaz and D. Shvarts, Model mean field self-similar solutions to the asymptotic evolution of Rayleigh–Taylor and Richtmyer–Meshkov instabilities and its dependence on initial conditions, Phys. Plasmas **25**, 062126 (2018).

[13] J. R. Chasnov, On the decay of inhomogeneous turbulence, J. Fluid. Mech. **342**, 335 (1997).

[14] A. Llor, Invariants of free turbulent decay, arXiv:physics/0612220.

[15] O. Soulard, F. Guillois, J. Griffond, V. Sabelnikov, and S. Simoëns, Permanence of large eddies in Richtmyer–Meshkov turbulence with a small Atwood number, Phys. Rev. Fluids **3**, 104603 (2018).

[16] L. G. Loitsyanskii, Some basic laws of isotropic turbulent flow, Trudy Tsentr. Aero.-Giedrodin. Inst. **440**, 3 (1939).

[17] A. N. Kolmogorov, On the degeneration of isotropic turbulence in an incompressible viscous fluid, Dokl. Akad. Nauk. SSSR **31**, 538 (1941).

[18] L. D. Landau and E. M. Lifshitsz, *Continuum Mechanics* (Gostekhizdat, Moscou, 1954).

[19] P. G. Saffman, The large-scale structure of homogeneous turbulence, J. Fluid Mech. **27**, 581 (1967).

[20] A. Llor, Langevin equation of big structure dynamics in turbulence, Eur. J. Mech. B **30**, 480 (2011).

[21] P. A. Davidson, *Turbulence: An Introduction for Scientists and Engineers* (Oxford University Press, Oxford, UK, 2004).

[22] M. Lesieur, *Turbulence in Fluids*, 4th ed. (Springer, Berlin, 2008).

[23] M. Lesieur and S. Ossia, 3D isotropic turbulence at very high Reynolds numbers: EDQNM study, J. Turb **1**, N1 (2000).

[24] O. Soulard, J. Griffond, B.-J. Gréa, and G. Viciconte, Permanence of large eddies in decaying variable-density homogeneous turbulence with small mach numbers, Phys. Rev. Fluids **5**, 064613 (2020).

[25] J. G. Wouchuk and K. Nishihara, Linear perturbation growth at a shocked interface, Phys. Plasmas **3**, 3761 (1996).

[26] J. G. Wouchuk and K. Nishihara, Asymptotic growth in the linear Richtmyer-Meshkov instability, Phys. Plasmas **4**, 1028 (1997).

[27] D. L. Sandoval, The dynamics of variable density turbulence, Ph.D. thesis, Univ. Washington, 1995.

[28] D. Livescu and J. R. Ristorcelli, Buoyancy–driven variable–density turbulence, J. Fluid Mech. **591**, 43 (2007).

[29] D. Livescu and J. R. Ristorcelli, Variable–density mixing in buoyancy-driven turbulence, J. Fluid Mech. **605**, 145 (2008).

[30] D. Chung and D. I. Pullin, Direct numerical simulation and large-eddy simulation of stationary buoyancy-driven turbulence, J. Fluid Mech. **643**, 279 (2010).

[31] O. Soulard, J. Griffond, and D. Souffland, Pseudocompressible approximation and statistical turbulence modeling: Application to shock tube flows, Phys. Rev. E **85**, 026307 (2012).

[32] O. Soulard and J. Griffond, Inertial-range anisotropy in Rayleigh-Taylor turbulence, Phys. Fluids **24**, 025101 (2012).

[33] M. Meldi and P. Sagaut, On non-self-similar regimes in homogeneous isotropic turbulence decay, J. Fluid Mech. **711**, 364 (2012).

[34] G. Eyink and D. J. Thomson, Free decay of turbulence and breakdown of self-similarity, Phys. Fluids **12**, 477 (2000).

[35] G. Comte-Bellot and S. Corrsin, The use of a contraction to improve the isotropy of grid-generated turbulence, J. Fluid Mech. **25**, 657 (1966).

[36] M. Vandenboomgaerde, C. Mügler, and S. Gauthier, Impulsive model for the Richtmyer-Meshkov instability, Phys. Rev. E **58**, 1874 (1998).

[37] G. Dimonte, C. E. Frerking, and M. Schneider, Richtmyer–Meshkov Instability in the Turbulent Regime, Phys. Rev. Lett. **74**, 4855 (1995).

[38] S. W. Haan, Onset of nonlinear saturation for Rayleigh–Taylor growth in the presence of a full spectrum of modes, Phys. Rev. A **39**, 5812 (1989).

[39] S. W. Haan, Weakly nonlinear hydrodynamic instabilities in inertial fusion, Phys. Fluids B **3**, 2349 (1991).

[40] J. Garnier, C. Cherfils-Clérouin, and P.-A. Holstein, Statistical analysis of multimode weakly nonlinear Rayleigh-Taylor instability in the presence of surface tension, Phys. Rev. E **68**, 036401 (2003).

[41] J. Garnier and L. Masse, Statistical approach of weakly nonlinear ablative Rayleigh-Taylor instability, Phys. Plasmas **12**, 062707 (2005).

[42] G. Dimonte, A modal wave-packet model for the multi-mode Richtmyer-Meshkov instability, Phys. Fluids **33**, 014108 (2021).

[43] S. Shanmuganathan, D. L. Youngs, J. Griffond, B. Thornber, and R. J. R. Williams, Accuracy of high-order density-based compressible methods in low Mach vortical flows, Int. J. Numer. Meth. Fluids **74**, 335 (2013).

[44] A. Suresh and H. T. Huynh, Accurate monotonicity-preserving schemes with Runge-Kutta time stepping, J. Comput. Phys. **136**, 83 (1997).

[45] E. F. Toro, *Riemann Solvers and Numerical Methods for Fluid Dynamics*, 2nd ed. (Springer-Verlag, Berlin, 1997).

[46] B. Thornber, J. Griffond, O. Poujade, N. Attal, H. Varshochi, P. Bigdelou, P. Ramaprabhu, B. Olson, J. Greenough, Y. Zhou *et al.*, Late-time growth rate, mixing, and anisotropy in the multimode narrowband Richtmyer-Meshkov instability: The θ-group collaboration, Phys. Fluids **29**, 105107 (2017).

[47] T. Oggian, D. Drikakis, D. L. Youngs, and R. J. R. Williams, Computing multi-mode shock induced compressible turbulent mixing at late times, J. Fluid Mech. **779**, 411 (2015).

[48] M. Groom and B. Thornber, Direct numerical simulation of the multimode narrowband Richtmyer–Meshkov instability, Comput. Fluids **194**, 104309 (2019).

[49] M. Groom and B. Thornber, The influence of initial perturbation power spectra on the growth of a turbulent mixing layer induced by Richtmyer–Meshkov instability, Physica D: Nonlin. Phenom. **407**, 132463 (2020).

[50] P. Sagaut and C. Cambon, *Homogeneous Turbulence Dynamics* (Springer, Berlin, 2018).

[51] G. I. Barenblatt, Self-similar turbulence propagation from an instantaneous plane source, in *Nonlinear Dynamics and Turbulence*, edited by G. I. Barenblatt, G. Iooss, and D. D. Joseph (Pitman, Boston, 1983), pp. 48–60.

[52] J. D. Ramshaw, Simple model for linear and nonlinear mixing at unstable fluid interfaces with variable acceleration, Phys. Rev. E **58**, 5834 (1998).

[53] O. Sadot, U. Alon, D. Oron, L. A. Levin, G. Erez, G. Ben-Dor, and D. Shvarts, Study of Non-Linear Evolution of Single-Mode and Two-Bubble Interaction Under Richtmyer–Meshkov Instability, Phys. Rev. Lett. **80**, 1654 (1998).

[54] A. Rikatani, U. Alon, and D. Shvarts, Vortex model for the nonlinear evolution of the multimode Richtmyer–Meshkov instability at low Atwood numbers, Phys. Rev. E **58**, 7410 (1998).

[55] M. Boulet and J. Griffond, Ttriclade: Influence d'une instabilité sinueuse sur les instabilités de Richtmyer–Meshkov en 2D et 3D, Technical report, CEA, DAM, DIF (2004).

[56] M. Meldi and P. Sagaut, Turbulence in a box: Quantification of large-scale resolution effects in isotropic turbulence free decay, J. Fluid Mech. **818**, 697 (2017).

[57] B. Thornber, Impact of domain size and statistical errors in simulations of homogeneous decaying turbulence and the Richtmyer–Meshkov instability, Phys. Fluids **28**, 045106 (2016).